The Astrophysical Journal, 924:45 (20pp), 2022 January 10 https://doi.org/10.3847/1538-4357/ac33b5
© 2022. The Author(s). Published by the American Astronomical Society.
OPEN ACCESS

Observational Constraints on the Maximum Energies of Accelerated Particles in Supernova Remnants: Low Maximum Energies and a Large Variety

Hiromasa Suzuki[1,2], Aya Bamba[1,3], Ryo Yamazaki[4,5], and Yutaka Ohira[6]
[1] Department of Physics, The University of Tokyo, 7-3-1 Hongo, Bunkyo-ku, Tokyo 113-0033, Japan; hiromasa050701@gmail.com
[2] Department of Physics, Faculty of Science and Engineering, Konan University, 8-9-1 Okamoto, Higashinada, Kobe, Hyogo 658-8501, Japan
[3] Research Center for the Early Universe, The University of Tokyo, 7-3-1 Hongo, Bunkyo-ku, Tokyo 113-0033, Japan
[4] Department of Physics and Mathematics, Aoyama Gakuin University, 5-10-1 Fuchinobe, Chuo-ku, Sagamihara, Kanagawa 252-5258, Japan
[5] Institute of Laser Engineering, Osaka University, 2-6 Yamadaoka, Suita, Osaka 565-0871, Japan
[6] Department of Earth and Planetary Science, The University of Tokyo, 7-3-1 Hongo, Bunkyo-ku, Tokyo 113-0033, Japan
Received 2021 September 22; revised 2021 October 25; accepted 2021 October 25; published 2022 January 11

Abstract

Supernova remnants (SNRs) are thought to be the most promising sources of Galactic cosmic rays. One of the principal questions is whether they are accelerating particles up to the maximum energy of Galactic cosmic rays (∼PeV). In this work, a systematic study of gamma-ray-emitting SNRs is conducted as an advanced study of Suzuki et al. Our purpose is to newly measure the evolution of maximum particle energies with increased statistics and better age estimates. We model their gamma-ray spectra to constrain the particle-acceleration parameters. Two candidates of the maximum energy of freshly accelerated particles, the gamma-ray cutoff and break energies, are found to be well below PeV. We also test a spectral model that includes both the freshly accelerated and escaping particles to estimate the maximum energies more reliably, but no tighter constraints are obtained with current statistics. The average time dependences of the cutoff energy ($\propto t^{-0.81\pm0.24}$) and break energy ($\propto t^{-0.77\pm0.23}$) cannot be explained with the simplest acceleration condition (Bohm limit) and require shock–ISM (interstellar medium) interaction. The average maximum energy during lifetime is found to be $\lesssim$20 TeV $(t_M/1\ \mathrm{kyr})^{-0.8}$ with t_M being the age at the maximum, which reaches PeV if $t_M \lesssim 10$ yr. The maximum energies during lifetime are suggested to have a variety of 1.1–1.8 dex from object to object. Although we cannot isolate the cause of this variety, this work provides an important clue to understanding the microphysics of particle acceleration in SNRs.

Unified Astronomy Thesaurus concepts: Supernova remnants (1667); Galactic cosmic rays (567); Gamma-ray sources (633); Cosmic ray sources (328); X-ray sources (1822)

1. Introduction

Galactic cosmic rays are high-energy particles that have an energy distribution approximated by a power-law function with a maximum energy of $\approx 10^{15.5}$ eV (≈3 PeV) and an energy density of ∼1 eV cm^{-3} (Gloeckler & Jokipii 1967). Although it has been more than 100 yr from their discovery, their acceleration sites are still unclear. Supernova remnants (SNRs) are thought to be the most promising sources that can provide such a high maximum energy and large energy density. According to analytical models of diffusive shock acceleration, they are believed to supply particles with energies of $\lesssim$PeV (e.g., Bell 1978; Lagage & Cesarsky 1983).

Gamma-ray observations have revealed that charged particles are accelerated to energies above TeV (10^{12} eV) in young ($\lesssim$2 kyr) SNRs (e.g., Cassiopeia A by Ahnen et al. 2017; Tycho by Giordano et al. 2012; RX J1713.7−3946 by H.E.S.S. Collaboration et al. 2018). Most of these SNRs, however, feature spectral turnovers at energies below PeV. Recent Tibet air shower array and LHAASO (Large High Altitude Air Shower Observatory) observations have successfully identified a number of PeVatron candidates (Amenomori et al. 2021; Cao et al. 2021), which include only a few SNRs. These results suggest that very-high-energy particles accelerated in young evolutionary stages have already escaped from the SNRs (Ptuskin & Zirakashvili 2003, 2005; Ptuskin et al. 2008; Caprioli et al. 2009; Ohira et al. 2010, 2011; Bell et al. 2013; Nava et al. 2016; Celli et al. 2019), or that SNRs simply cannot accelerate particles up to PeV. Other scenarios have also been proposed in which SNRs in specific conditions are PeVatrons, e.g., SNRs with pulsars by Ohira et al. (2018), very young SNRs in dense environments by Schure & Bell (2013), Marcowith et al. (2018), Cristofari et al. (2020), and Inoue et al. (2021). In any case, evaluation of maximum energies of fleshly accelerated particles by isolating the contribution of particles that are no longer accelerated will be essential to examining whether SNRs are PeVatrons or not.

Given that evolution of the maximum attainable energies of the particle-acceleration processes is unknown, studying individual SNRs is insufficient to determine their maximum energies during their lifetime. A systematic study with a large number of SNRs is required to extract their global trends. In such a study, reliability of their ages is very important yet was not taken into account in previous studies (Zeng et al. 2019; Suzuki et al. 2020b). Suzuki et al. (2021) investigated the reliability of the age estimates and concluded that a systematic uncertainty of a factor of four is associated with the SNR ages except for a limited number of systems where more reliable estimations are possible.

In this work, a systematic study of gamma-ray-emitting SNRs is conducted as an advanced study of Suzuki et al. (2020b) with increased statistics and better age estimates. We especially aim to evaluate their maximum attainable energies during lifetime and their dependence on environments.

Original content from this work may be used under the terms of the Creative Commons Attribution 4.0 licence. Any further distribution of this work must maintain attribution to the author(s) and the title of the work, journal citation and DOI.

Our sample consists of 38 SNRs. This is described in Section 2. We analyze the latest data obtained with Fermi-LAT to extract the energy spectra of 15 SNRs out of 38 with the best statistics available. This is described in Appendix A. A systematic spectral modeling of the gamma-ray data is performed for all the 38 SNRs, and then systematic trends and dispersions of the gamma-ray parameters are summarized (Section 3). We show that their current maximum energies are indicated to be well below PeV. Particle-acceleration parameters, including the maximum energies and spectral indices, are discussed in Section 4. Here, we argue that SNRs still can be PeVatrons under certain conditions. Throughout the paper, errors in text, figures, and tables indicate a 1σ confidence range unless mentioned otherwise.

2. Sample and Estimation of Age

The SNRs considered in this work are selected from the objects either in the first Fermi-LAT SNR catalog (Acero et al. 2016; 30 SNRs) or a preceding systematic gamma-ray study of SNRs (Zeng et al. 2019; 35 SNRs). Among them, the sample of this work consists of objects with individually published gamma-ray spectra. The resultant 38 SNRs are listed in Table 1.

Two age estimates, plasma age $t_{\rm p}$ and dynamical age $t_{\rm dyn}$, are obtained primarily based on X-ray observations as follows. Thermal electron number density $n_{\rm e}$ is used if available.[7] For those either with ionizing plasmas or recombining plasmas, the ionization or recombination timescales $n_{\rm e}t$, respectively, are also extracted from the literature. Then, the plasma age $t_{\rm p}$ is calculated by dividing $n_{\rm e}t$ with $n_{\rm e}$.[8] The dynamical age $t_{\rm dyn}$, which is determined based on shock dynamics (from a combination of the parameters, SNR diameter D[9], shock speed, $n_{\rm e}$, etc.), estimated in previous works is also used. For objects whose reliable age estimations are available (historical age, light-echo age, kinematic age of associated neutron star, and kinematic age of ejecta knots; summarized in Suzuki et al. 2021), we adopt these values (referred to as $t_{\rm r}$).

For each object, the most reliable age, that is, the "best age", t_b is defined, and it is used in our analysis below. If available, we assume $t_{\rm r}$ as the best age estimate ($t_b = t_{\rm r}$). If only $t_{\rm p}$ and $t_{\rm dyn}$ are available and these are consistent within a factor of four, $t_{\rm p}$ is chosen since these two have no significant difference (Suzuki et al. 2021). In the following two cases, these two ages are different by more than a factor of four: RX J1713.7−3946 and W 51 C. For RX J1713.7−3946, its plasma age $t_{\rm p}$ is too large considering its large shock velocities observed and bright X-ray and gamma-ray emissions. Thus, $t_{\rm dyn}$ is chosen as the best age. This is probably because the object has almost completely nonthermal X-ray emission and its thermal X-ray emission has been barely detected only from a small region, thus the plasma parameters derived may not be reliable (Katsuda et al. 2015). For W 51 C, as Sasaki et al. (2014) mention, $t_{\rm p}$ is probably too large because of a wrong estimation of the density. Thus $t_{\rm dyn}$ is adopted as t_b. In the case where only $t_{\rm dyn}$ is known, it is used as t_b. These parameters are summarized in Table 2.

[7] The number density $n_{\rm e}$ is calculated based on a thermal X-ray emission measure and an assumption of the X-ray-emitting volume.

[8] The timescale $n_{\rm e}t$ is estimated from an X-ray spectroscopy. Basically, we use $n_{\rm e}t$ for the whole SNR. For SNRs with $n_{\rm e}t$ measured only for divided regions, we calculate their average values.

[9] The diameter D is calculated based on the Green's SNR catalog (Green 2019a, 2019b) with individual publications for distances (see Table 2).

Table 1
Gamma-ray-emitting SNRs Used in This Work[a]

SNR	GeV	TeV
Cassiopeia A (G111.7−2.1)	✓	✓
CTB 109 (G109.1−1.0)	This work	…
CTB 37 B (G348.7+0.3)	✓	✓
Cygnus loop (G74.0−8.5)	This work	…
G349.7+0.2	✓	✓
Gamma-cygni (G78.2+2.1)	✓	✓
Kes 79 (G33.6+0.1)	This work	…
MSH 11-62 (G291.0−0.1)	This work	…
MSH 11-56 (G326.3−01.8)	This work	…
Puppis A (G260.4−3.4)	✓	upper limits
RCW 103 (G332.4−0.4)	This work	…
RCW 86 (G315.4−2.3)	✓	✓
RX J1713-3946 (G347.3−0.5)	✓	✓
SN 1006 (G327.6+14.6)	✓	✓
Tycho (G120.1+1.4)	This work	✓
W 51 C (G49.2−0.7)	✓	✓
3C 391 (G31.9+0.0)	This work	…
CTB 37 A (G348.5+0.1)	✓	✓
G166.0+4.3	This work	…
G359.1−0.5	✓	✓
HB 21 (G89.0+4.7)	✓	…
HB 9 (G160.9+2.6)	This work	…
IC 443 (G189.1+3.0)	✓	✓
Kes 17 (G304.6+0.1)	This work	…
W 28 (G6.4−0.1)	✓	✓
W 44 (G34.7−0.4)	✓	…
W 49 B (G43.3−0.2)	✓	✓
CTB 33 (G337.0−0.1)	✓	…
G150.3+4.5	✓	…
G24.7+0.6	✓	✓
G353.6−0.7	✓	✓
G73.9+0.9	This work	…
HB 3 (G132.7+1.3)	✓	…
Monoceros nebula (G205.5+0.5)	This work	…
Vela Jr. (RX J0852.0-4622; G266.2−1.2)	✓	✓
S 147 (G180.0−1.7)	This work	…
W 30 (G8.7−0.1)	✓	…
W 41 (G23.3−0.3)	This work	✓

Note.
[a] Checkmarks indicate detections with Fermi-LAT (GeV band) or the ground-based observatories (TeV band), whereas "This work" indicates the objects whose Fermi-LAT data are analyzed in Appendix A. The references are presented in Table 2.

Figure 1 shows the diameter D and inferred shock velocity $v_{\rm ave}$ as a function of t_b. We calculate this velocity assuming the Sedov model as $v_{\rm ave} = D/5t_b$. A representative Sedov model, for which a condition $D = C_D t^{2/5}$ is assumed and the parameter C_D is selected by eye to roughly match the observations, is also plotted in Figure 1. Both the D–t_b and $v_{\rm ave}$–t_b plots are roughly consistent with the representative Sedov model within a factor of four, indicating that the estimated age t_b is plausible.[10]

3. Analysis and Results

3.1. Analysis

Here, a systematic analysis of the gamma-ray spectra obtained in Appendix A and those in the literature is conducted. The analysis is performed as follows. Here,

[10] See Suzuki et al. (2021) for more details of the reliability of ages.

Table 2
Properties of the SNRs Used in This Study

Name	D (pc)	Distance (kpc)	n_e (cm^{-3})	t_{dyn} (kyr)	t_p (kyr)	t_b (kyr)[a]
Cassiopeia A (G111.7−2.1)	4.9	3.4	6	0.48 (0.43–0.52)	1.1	0.340 (historical)
CTB 109 (G109.1−1.0)	24	2.79	1.1	14 (12–16)	18 (3.5–35)	$=t_p$
CTB 37 B (G348.7+0.3)	40	13.2	2	4.9	1.1 (0.63–2.5)	$=t_p$
Cygnus loop (G74.0−8.5)	31 (25–36)	0.54	2	18 (9–36)	13	$=t_p$
G349.7+0.2	7.5 (6.7–8.4)	11.5	4.2	1.5	1.3 (1.1–1.7)	$=t_p$
Gamma-cygni (G78.2+2.1)	26	2.5	0.24	8 (6.8–10)	3.2	$=t_p$
Kes 79 (G33.6+0.1)	19	7	1	12 (5.4–15)	2 (1.9–2)	$=t_p$
MSH 11-62 (G291.0−0.1)	20 (19–22)	5	0.16	1.2	3 (2.6–3.4)	$=t_p$
MSH 11-56 (G326.3−01.8)	45	4.1	0.15	16	30 (26–34)	$=t_p$
Puppis A (G260.4−3.4)	35 (32–38)	2.2	1	3.7 (3.4–4)	7.4 (7.1–7.9)	4.58 (4.01–5.15) (NS kinematic)
RCW 103 (G332.4−0.4)	10	3.3	5.7	3.2	3.4	$=t_p$
RCW 86 (G315.4−2.3)	30	2.5	2	1.3 (0.85–5.2)	1.1 (0.32–1.9)	1.835 (historical)
RX J1713-3946 (G347.3−0.5)	18 (16–19)	1	0.1	1.8 (1.6–2.1)	1.6 (1.3–1.9) × 10^2	$=t_{dyn}$
SN 1006 (G327.6+14.6)	18	2.2	0.15	1.7 (1.7–1.8)	5.2 (4.5–6)	1.014 (historical)
Tycho (G120.1+1.4)	6.6	3	0.13	1 (0.8–1.3)	0.073 (0–0.073)	0.448 (historical)
W 51 C (G49.2−0.7)	48	4.3	0.07	30	1.2 (0.61–1.9) × 10^2	$=t_{dyn}$
3C 391 (G31.9+0.0)	18 (16–21)	7.2	0.9	4.5 (4–5)	45 (38–49)	$=t_p$
CTB 37 A (G348.5+0.1)	44	7.9	0.8	24	52 (48–64)	$=t_p$
G166.0+4.3	66 (51–80)	4.5	0.9	24	69 (65–75)	$=t_p$
G359.1−0.5	28	3.29	0.7	70	19 (17–21)	$=t_p$
HB 21 (G89.0+4.7)	52 (45–60)	2.13	0.06	11 (10–12)	1.7 (1.1–2.5) × 10^2	$=t_p$
HB 9 (G160.9+2.6)	30	0.54	0.9	10 (0.8–20)	20 (19–22)	$=t_p$
IC 443 (G189.1+3.0)	20	1.8	1.6	4	12 (11–13)	>12.6 (NS kinematic)
Kes 17 (G304.6+0.1)	35	10	0.9	21 (2–40)	57 (46–78)	$=t_p$
W 28 (G6.4−0.1)	28	3.45	1	42	35 (32–41)	$=t_p$
W 44 (G34.7−0.4)	28 (24–31)	2.66	1	80 (60–100)	20 (18–23)	18.6 (14.9–22.4) (NS kinematic)
W 49 B (G43.3−0.2)	8 (7–9)	10	2.7	5.5 (5–6)	5.2 (4.7–5.7)	$=t_p$
CTB 33 (G337.0−0.1)	5.1	11	…	…	…	…
G150.3+4.5	19	0.4	…	…	…	…
G24.7+0.6	33 (22–44)	2.73	…	9.5	…	$=t_{dyn}$
G353.6−0.7	28	3.49	…	…	…	…
G73.9+0.9	32	4	…	12 (11–12)	…	$=t_{dyn}$
HB 3 (G132.7+1.3)	53	2.2	0.32	30 (27–33)	…	$=t_{dyn}$
Monoceros nebula (G205.5+0.5)	100	1.13	0.003	30	…	$=t_{dyn}$
Vela Jr. (RX J0852.0-4622; G266.2−1.2)	7	3.8	0.03	3.9 (0–3.9)	…	$=t_{dyn}$
S 147 (G180.0−1.7)	68	0.38	…	…	…	114 (80.9–147) (NS kinematic)
W 30 (G8.7−0.1)	52	4.15	0.15	32 (27–36)	…	$=t_{dyn}$
W 41 (G23.3−0.3)	33	3.38	…	1.3 (0.60–2.0) × 10^2	…	59.8 (49.1–70.4) (NS kinematic)

Note. Reference for (D; t_{dyn}; n_e and/or t_p; t_b; gamma-ray spectrum; distance): Cassiopeia A: (Green 2019a, 2019b; Reed et al. 1995;Patnaude & Fesen 2009;Murray et al. 1979;Green & Stephenson 2003;Ahnen et al. 2017; Reed et al. 1995; CTB 109: (Green 2019a; Green 2019b; Zhao et al. 2020;Sasaki et al. 2013; Castro et al. 2012;Zhao et al. 2020; ;);CTB 37 B: (Green 2019a, 2019b; Caswell et al. 1975;Aharonian et al. 2008a; Xin et al. 2016;Caswell et al. 1975);Cygnus loop: (Green 2019a, 2019b; Blair et al. 2005;Rappaport et al. 1974;Miyata et al. 1994; Katagiri et al. 2011;Blair et al. 2005);G349.7+0.2: (Green 2019a, 2019b; Tian & Leahy 2014; Slane et al. 2002; Ergin et al. 2015; H.E.S.S. Collaboration et al. 2015a;Tian & Leahy 2014);Gamma-cygni: (Green 2019a, 2019b; Higgs et al. 1977; Lozinskaya et al. 2000;Leahy et al. 2013; Hui et al. 2015;Fraija & Araya 2016; Aliu et al. 2013;Higgs et al. 1977; Lozinskaya et al. 2000);Kes 79: (Green 2019a, 2019b; Case & Bhattacharya 1998;Giacani et al. 2009; Sun et al. 2004; Auchettl et al. 2014;Case & Bhattacharya 1998);MSH 11-62: (Green 2019a, 2019b; Moffett et al. 2001; 2002;Slane et al. 2012; Moffett et al. 2001, 2002);MSH 15-56: (Green 2019a, 2019b; Rosado et al. 1996;Temim et al. 2013;Cesur et al. 2019 ; Temim et al. 2013;Rosado et al. 1996);Puppis A: (Green 2019a, 2019b; Reynoso et al. 2003; Winkler et al. 1988; Petre et al. 1982; this work H.E.S.S. Collaboration et al. 2015b Reynoso et al. 2003); RCW 103: (Green 2019a, 2019b; Carter et al. 1997; Braun et al. 2019; Xing et al. 2014; Carter et al. 1997); RCW 86: (Green 2019a, 2019b; Rosado et al. 1996; Sollerman et al. 2003; Williams et al. 2011; Lemoine-Goumard et al. 2012; Green & Stephenson 2003; Yuan et al. 2014; Rosado et al. 1996; Sollerman et al. 2003); RX J1713−3946: (Green 2019a, 2019b; Fukui et al. 2003; Tsuji & Uchiyama 2016; Katsuda et al. 2015; H.E.S.S. Collaboration et al. 2018); SN 1006: (Green 2019a, 2019b; Winkler et al. 2003; Winkler et al. 2014; Yamaguchi et al. 2008; Green & Stephenson 2003; Condon et al. 2017; Acero et al. 2010); Tycho: (Green 2019a, 2019b; Tian & Leahy 2011; Hayato et al. 2010; Hughes 2000; Hwang et al. 2002; Green & Stephenson 2003; Giordano et al. 2012; Acciari et al. 2011); W 51 C: (Green 2019a, 2019b; Koo & Moon 1997a, 1997b; Green et al. 1997; Koo et al. 1995; Sasaki et al. 2014; Koo et al. 1995; Jogler & Funk 2016); 3C 391: (Green 2019a, 2019b; Radhakrishnan et al. 1972; Chen & Slane 2001; Sato et al. 2014; Ergin et al. 2014); CTB 37 A: (Green 2019a, 2019b; Tian & Leahy 2012; Yamauchi et al. 2014; Abdollahi et al. 2020); G166.0+4.3: (Green 2019a, 2019b; Zhao et al. 2020; Burrows & Guo 1994; Matsumura et al. 2017; Araya 2013); G359.1−0.5: (Green 2019a, 2019b; Wang et al. 2020; Ohnishi et al. 2011; Suzuki et al. 2020a; Aharonian et al. 2008b; Hui et al. 2016); HB 21: (Green 2019a, 2019b; Zhao et al. 2020; Lazendic & Slane 2006; Suzuki et al. 2018; Ambrogi et al. 2019); HB 9: (Green 2019a, 2019b; Zhao et al. 2020; Leahy & Aschenbach 1995; Sezer et al. 2019; Araya 2014); IC 443: (Green 2019a, 2019b; Zhao et al. 2020; Troja et al. 2008; Matsumura 2018; this work Ackermann et al. 2013); Kes 17: (Green 2019a, 2019b; Caswell et al. 1975; Gelfand et al. 2013; Washino et al. 2016); W 28: (Green 2019a, 2019b; Wang et al. 2020; Li & Chen 2010; Okon et al. 2018; Cui et al. 2018); W 44: (Green 2019a, 2019b; Wang et al. 2020; this work; Uchida et al. 2012; this work Ackermann et al. 2013); W 49 B: (Green 2019a, 2019b; Moffett & Reynolds 1994; Zhou & Vink 2018; Matsumura 2018; H.E.S.S. Collaboration et al. 2018); CTB 33: (Green 2019a, 2019b; Sarma et al. 1997; …; …; Castro et al. 2013); G150.3+4.5: (Green 2019a, 2019b; Cohen 2016; …; …; Ackermann et al. 2017); G24.7+0.6: (Green 2019a, 2019b; Wang et al. 2020; Leahy 1989; …; MAGIC Collaboration et al. 2019);G353.6−0.7: (Green 2019a, 2019b; Wang et al. 2020; …; Doroshenko et al. 2017; …; Condon et al. 2017); G73.9+0.9: (Green 2019a, 2019b; Wang et al. 2020; Lozinskaya et al. 1993; …; Zdziarski et al. 2016; Pavlović et al. 2013); HB 3: (Green 2019a, 2019b; Routledge et al. 1991; Lazendic & Slane 2006; Katagiri et al. 2016b); Monoceros nebula: (Green 2019a, 2019b; Zhao et al. 2020; Leahy et al. 1986; Katagiri et al. 2016a); Vela Jr.: (Green 2019a, 2019b; Katsuda et al. 2008; Slane et al. 2001; …; Aharonian et al. 2007; Tanaka et al. 2011); S 147: (Green 2019a, 2019b; Zhao et al. 2020; …; …; … this work; Katsuta et al. 2012); W 30: (Green 2019a, 2019b; Wang et al. 2020; Finley & Oegelman 1994; Ajello et al. 2012); W 41: (Misanovic et al. 2011; Tian et al. 2007; this work H.E.S.S. Collaboration et al. 2015c; Leahy & Tian 2008).

[a] "Historical" and "NS kinematic," respectively, indicate that the age t_b is based on a historical document and kinematics of an associated neutron star (see Suzuki et al. 2021 for details).

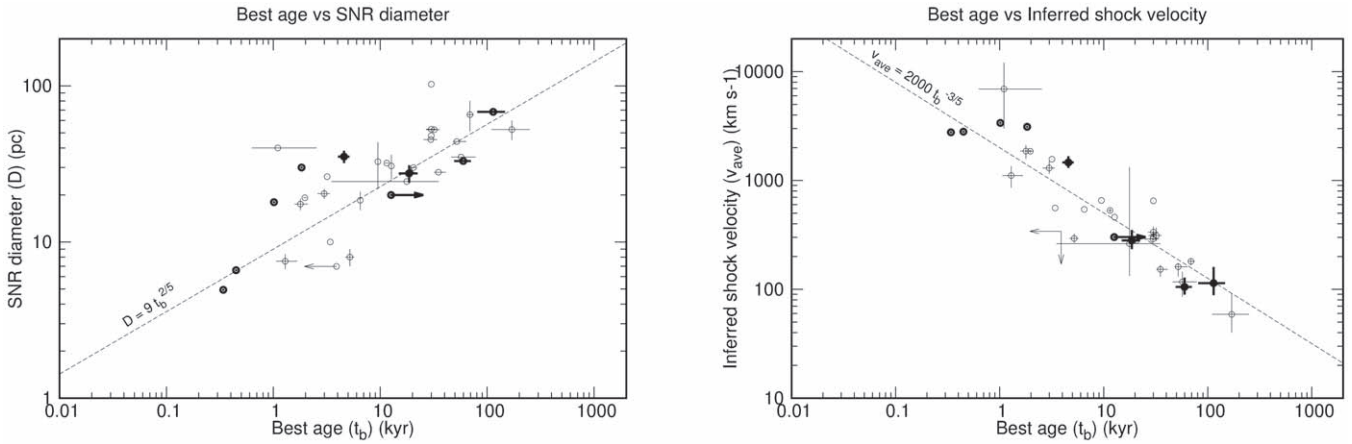

Figure 1. Left and right panels show the SNR diameter D and inferred shock velocity $v_{\rm ave}$ as a function of t_b, respectively. See Section 2 for the definition of the "best age" t_b. The velocity $v_{\rm ave}$ is calculated as $v_{\rm ave} = D/5t_b$. Thick and thin crosses represent the SNRs with and without t_r, respectively. A representative Sedov model, for which a condition $D = C_D t^{2/5}$ is assumed with a parameter C_D selected by eye to roughly match the observations, is also plotted with black-dashed lines.

hadronic emissions originating from protons are assumed to dominate the gamma-ray spectra, which seems to be true at least for several SNRs based on their spectral shapes and energetics (e.g., Ackermann et al. 2013). The exponential cutoff energies ($E_{\rm cut}$) or break energies ($E_{\rm br}$) of the gamma-ray spectra reflect the maximum energies of freshly accelerated particles (Ohira et al. 2011; Celli et al. 2019; Brose et al. 2020). Assuming that particles that are no longer accelerated do not significantly contribute to gamma-rays[11], we expect exponential-like cutoff features. However, if the emission of escaping particles is significant as well, the gamma-ray spectra will be approximated with a broken power-law model.[12] Since we cannot generally distinguish between these two situations without detailed properties of acceleration sites, the gamma-ray spectra are fitted with both an exponential cutoff power-law model,

$$\frac{dN}{dE} = {\rm A}\,(E/1\ {\rm GeV})^{-\Gamma_{\rm cut}} \exp(-E/E_{\rm cut}), \tag{1}$$

and a broken power-law model,

$$\frac{dN}{dE} = \begin{cases} {\rm A}\,(E/E_{\rm br})^{-\Gamma_{\rm br,low}} & (E < E_{\rm br}) \\ {\rm A}\,(E/E_{\rm br})^{-\Gamma_{\rm br,high}} & (E \geqslant E_{\rm br}), \end{cases} \tag{2}$$

where A is a normalization factor.

Note that only the energy spectra are used for modeling instead of using the spatial distributions as well including nearby sources, as in the case of the Fermi-LAT data analysis (Appendix A). This is an approximate method since the populations of spectral data points are all assumed to follow the Gaussian distributions independently. This approximation is adopted to combine the Fermi-LAT data with those taken with other gamma-ray observatories.[13] In this analysis, upper-limits are also included, assuming that they follow a Gaussian probability distribution with the zero mean and standard deviation corresponding to the upper-limit value.

In this work, the Markov Chain Monte Carlo (MCMC) algorithm is adopted to find the best-fit spectral parameters and their confidence ranges. MCMCs are particularly useful in Bayesian inference because the posterior distributions are often difficult to work with via analytical examination. In these cases, MCMCs give approximate aspects of posterior distributions that cannot be directly calculated (e.g., posterior means and standard deviations).

In our spectral analysis below, the "Random Walk Metropolis-Hasting" algorithm is used. Let μ^i denote a d-dimensional vector of the model parameter values at stage i of the iteration. A candidate (proposal) of the next parameter set μ^* is defined as

$$\mu^* = \mu^i + c\Sigma^{1/2} W, \tag{3}$$

where c and Σ are a scaling parameter and covariance matrix, respectively, and $W \sim N\,(0, I_d)$. With a parameter α, which is defined as

$$\alpha = \min\{1, p(\mu^*|D)/p(\mu^i|D)\}, \tag{4}$$

whether the proposal is accepted or rejected is determined as

$$\mu^{i+1} = \begin{cases} \mu^* & (Z < \alpha) \\ \mu^i & ({\rm else}), \end{cases} \tag{5}$$

where $Z \sim {\rm Unif}\ (0, 1)$. Thus, if the likelihood of the proposal state is smaller than the current value, the proposal is rejected with a 100% probability. In the opposite case, the proposal is accepted with a certain probability.

The algorithm adopted in this work is constructed utilizing a C++ library MCMCLib.[14] In order to sample parameters properly, the scaling parameter of the proposal state c is optimized for each run to get the average acceptance rate of $\approx$0.5. The delta χ^2 method is combined to MCMCs due to difficulties in determining accurate probability distributions of $E_{\rm cut}$, $E_{\rm br}$, and $\Gamma_{\rm br,high}$ with one MCMC run due to broad parameter ranges to be searched and local minima. In the delta χ^2 method, searches for confidence regions of parameters are based on the difference between the best and current likelihood,

[11] Note that a certain amount of particles that are no longer accelerated and thus have higher energies than the current maximum energy of particles may still be in downstream and contribute to the gamma-ray emission. Here, their contribution is ignored.

[12] Physically, they will have cutoff features above the breaks as well, but these will be hardly visible with current statistics.

[13] Most of the data taken with the ground-based gamma-ray observatories are not accessible to the public, so that only the energy spectra made after data reduction and analysis presented in publications are available.

[14] https://github.com/kthohr/mcmc

$-2\log(\Delta L) \approx \Delta\chi^2$. We run an MCMC for a fixed ($E_{\rm cut}$, $E_{\rm br}$, $\Gamma_{\rm br,high}$) set with the other parameters kept free. This process is repeated to cover all the sets of ($E_{\rm cut}$, $E_{\rm br}$, $\Gamma_{\rm br,high}$) within their parameter-search ranges. Considering non-Gaussian probability distributions of $E_{\rm cut}$ and $E_{\rm br}$, we calculate 2σ confidence ranges for them. Iteration number of each MCMC run is 10^5, and we use the last 10^4 iterations to create parameter histograms.

3.2. Results

The best-fit parameters are presented in Table 3. For $E_{\rm cut}$ and $E_{\rm br}$, 2σ errors are presented. While $E_{\rm cut}$ is constrained well for most of the sample, $E_{\rm br}$ cannot be determined for eight objects. The objects with bad fits (if the null hypothesis probability is lower than 0.2%) are excluded because their spectra are regarded as not being explained well.

Overall, our results are consistent with Suzuki et al. (2020b) and are better constrained with better statistics. Figures 2(a) and (b) show the plots of $E_{\rm cut}$ and $E_{\rm br}$ over the age t_b, respectively. Both of them show decreasing trends with age, which are consistent with Zeng et al. (2019) and Suzuki et al. (2020b). These $E_{\rm cut}$–t_b and $E_{\rm br}$–t_b plots are fitted with a power-law model, and the best-fit functions are obtained as $E_{\rm cut} = 1.3\,(0.67\text{–}2.4)\ {\rm TeV}\ (t_b/1\ {\rm kyr})^{-0.81\pm0.24}$ and $E_{\rm br} = 270\,(140\text{–}510)\ {\rm GeV}\ (t_b/1\ {\rm kyr})^{-0.77\pm0.23}$. These functions and their 1σ confidence ranges are overplotted with gray regions. The cutoff energies might show two distinct populations, one of which is ∼0.1–1 TeV (e.g., RX J1713.7 −3946) and the other is ∼1–100 GeV (e.g., Cygnus Loop). Note that $E_{\rm cut}$ roughly corresponds to the highest gamma-ray energies whereas $E_{\rm br}$ is sometimes lower, especially in the case where another curvature is required below the highest energies.

The spectral indices of the broken power-law model, $\Gamma_{\rm br,low}$ and $\Gamma_{\rm br,high}$, are plotted in Figure 3. Distribution of the indices, $\Gamma_{\rm br,low}$ and $\Gamma_{\rm br,high}$, are found to be 2.2 ± 0.4 and 2.9 ± 0.7, respectively.[15] The difference between these two, $\Gamma_{\rm br,high} - \Gamma_{\rm br,low}$, is calculated as 0.74 ± 0.51. The spectral index of the cutoff power-law model, $\Gamma_{\rm cut}$ have a distribution of 2.0 ± 0.4 (Figure 3).

In addition to $E_{\rm cut}$ and $E_{\rm br}$, two important parameters are introduced, namely the hardness ratio (ratio of the 10 GeV to 100 TeV and the 1–10 GeV luminosities; hereafter $R_{\rm GeV}$) and the normalized gamma-ray luminosity ($\hat{L}$). The latter is the luminosity (1 GeV–100 TeV) normalized at 1 GeV, i.e.,

$$\hat{L} = \left(\int_{1\ {\rm GeV}}^{100\ {\rm TeV}} \frac{E\ dN\ (E)}{dE}\, dE \right) \Bigg/ \frac{E^2\ dN\,(1\ {\rm GeV})}{dE}. \quad (6)$$

Ideally, the quantity $\hat{L}$ is governed by the maximum energy of the gamma-rays from freshly accelerated particles $E_{{\rm max},\gamma}$ with a fixed spectral index of 2.0, and can be approximated as

$$\hat{L} \approx \ln(E_{{\rm max},\gamma}/1\ {\rm GeV}). \quad (7)$$

Figure 2 (c) and (d) show decreasing trends of $R_{\rm GeV}$ and $\hat{L}$ with increasing age t_b, respectively, corresponding to the decreases of $E_{\rm cut}$ and $E_{\rm br}$.

As seen in Figure 2, large dispersions of the gamma-ray parameters at the same ages are indicated. To evaluate these dispersions quantitatively, distributions of the dispersions as a function of age are plotted in Figure 4. We use the standard deviation of the values (e.g., $E_{\rm cut}$) as a measure of dispersion at individual age bins. The logarithmically divided age bins have a ∼1 dex width each, which is close to the uncertainties associated with the ages for most SNRs. These parameter distributions are generated as follows: randomized data plots (of, e.g., $E_{\rm cut}$–t_b) considering errors of individual data points are generated. For each plot, dispersions at individual age bins are calculated. This procedure is repeated for 10^4 times, and the mean and standard deviation are evaluated for each age bin. These correspond to the mean and 1σ error values plotted in Figure 4. As seen in Figure 4, dispersions of $E_{\rm cut}$ and $E_{\rm br}$ are found to be 1.1–1.8 and 1.1–1.6 orders of magnitude, respectively.

4. Discussion

Here, physical parameters of particle-acceleration environments, in particular, the maximum energies of freshly accelerated particles and spectral indices, are discussed.

4.1. Maximum Energies of Freshly Accelerated Particles

4.1.1. Simply Based on Observations

We have derived the systematic trends approximated with a power-law function, $E_{\rm cut} = 1.3\,(0.67\text{–}2.4)\ {\rm TeV}\ (t_b/1\ {\rm kyr})^{-0.81\pm0.24}$ and $E_{\rm br} = 270\,(140\text{–}510)\ {\rm GeV}\ (t_b/1\ {\rm kyr})^{-0.77\pm0.23}$. With an assumption that either of these corresponds to the maximum energy of the gamma rays from freshly accelerated particles, we can conclude that the maximum energies of freshly accelerated particles are far below PeV. It is possible, however, that these results are biased due to the contribution of particles that are no longer accelerated. We consider this possibility in detail in the next section.

4.1.2. Based on a Combination of Observations and Theoretical Predictions

Here we use a spectral model that takes into account the contribution of escaping particles to constrain the freshly accelerated particles' maximum energies more reliably. The model spectrum for total gamma-ray emission is defined as

$$\frac{dN}{dE} = \begin{cases} {\rm A}_1\, E^{-\mu_{\rm acc}} & (E < E_{\rm bc,br}) \\ {\rm A}_2\, E^{-\mu_{\rm esc}} \exp(-E/E_{\rm bc,\,cut}) & (E \geqslant E_{\rm bc,br}), \end{cases} \quad (8)$$

where $\mu_{\rm acc}$, $\mu_{\rm esc}$, $E_{\rm bc,br}$, and $E_{\rm bc,cut}$ are the spectral indices of accelerated particles and escaping particles, and break and cutoff energies, respectively. A condition ${\rm A}_1 = E_{\rm bc,br}^{\mu_{\rm acc}-\mu_{\rm esc}} \exp(-E_{\rm bc,br}/E_{\rm bc,\,cut})\ {\rm A}_2$ is kept. This spectral model is described in Figure 5. We assume that the break energy $E_{\rm bc,br}$ is the best guess of the maximum energy $E_{{\rm max},\gamma}$, but it is still possible that this energy corresponds to that of confined particles that are no longer accelerated (Ohira et al. 2010, 2011; Celli et al. 2019; Brose et al. 2020). By contrast, the cutoff energy $E_{\rm bc,cut}$ corresponds to the maximum energy of confined particles, that of escaping particles that contribute to gamma-ray emission, or the highest energy of particles attained during lifetime (Ohira et al. 2010, 2011; Celli et al. 2019). We cannot distinguish between these possibilities with the current low statistics of the gamma-ray spectra and limited spatial resolutions.

[15] Errors indicate the standard deviations. Same for the other errors in this paragraph.

Table 3
Gamma-ray Spectral Parameters of Our SNR Sample

Name	$\Gamma_{\rm cut}$	$\Gamma_{\rm br,low}$	$\Gamma_{\rm br,high}$	$E_{\rm cut}$ (GeV)	$E_{\rm br}$ (GeV)	$L_{1-100\ \rm GeV}$[a]	$\hat{L}$	$R_{\rm GeV}$	χ^2 (d.o.f.)[b]	
									Cutoff	Broken
CassiopeiaA	2.11 (2.07–2.15)	2.13 (2.08–2.16)	3.10 (2.85–3.36)	$2.3\ (1.2–3.5)\times10^{3}$	$5.9\ (2.1–14)\times10^{2}$	$6.86\ (6.56–7.17)\times10^{34}$	4.89 (4.48–5.45)	1.4 (1.28–1.53)	22.6 (14)	21.9 (13)
CTB109	2.04 (1.98–2.15)	1.96 (1.51–2.26)	2.10 (1.21–3.96)	>23	⋯	$1.19\ (1.09–1.29)\times10^{34}$	4.98 (4.07–10.4)	1.28 (1.03–3.5)	9.8 (6)	8.86 (5)
CTB37B	2.00 (1.89–2.06)	1.73 (1.40–1.93)	2.41 (2.20–2.61)	$2.5\ (0.69–11)\times10^{3}$	60 (11–970)	$3.28\ (2.62–3.75)\times10^{35}$	7.32 (6.13–10.3)	2.16 (1.85–2.92)	20.1 (13)	15.9 (12)
Cygnus loop	2.11 (1.99–2.24)	2.18 (1.92–2.33)	2.80 (2.55–2.96)	11 (6.2–26)	3.1 (1.1–7.2)	$1.55\ (1.49–1.64)\times10^{33}$	1.85 (1.77–1.93)	0.127 (0.0963–0.179)	8.14 (5)	6.86 (4)
G349.7+0.2	2.27 (2.11–2.39)	2.26 (2.05–2.50)	2.81 (2.35–3.40)	$1.4\ (0.5–20)\times10^{3}$	<1500	$4.1\ (2.87–5.02)\times10^{35}$	3.07 (2.42–4.46)	0.782 (0.569–1.17)	9.43 (13)	9.78 (12)
Gamma-cygni	1.93 (1.82–2.03)	1.95 (1.87–2.05)	2.90 (2.40–3.96)	$3\ (1–16)\times10^{3}$	1.1 (8.5–4300)	$1.62\ (1.31–1.87)\times10^{34}$	10.1 (7.24–14.9)	2.99 (2.21–4.2)	27.7 (22)	26.2 (21)
Kes79	1.89 (1.07–2.42)	2.51 (2.05–2.71)	3.81 (2.80–3.96)	3.1 (1.3–1400)	⋯	$1.84\ (1.61–2.12)\times10^{35}$	1.31 (1.16–1.55)	0.0149 (0.00156–0.0699)	4.97 (5)	5.04 (4)
MSH11-62	1.55 (1.33–1.75)	2.06 (1.96–2.16)	3.91 (3.55–3.96)	7.4 (4.9–13)	11 (4.8–14)	$1.22\ (1.14–1.28)\times10^{35}$	3.14 (2.72–3.69)	0.187 (0.147–0.236)	7.73 (6)	11.1 (5)
MSH11-56	2.04 (1.95–2.11)	1.75 (1.35–1.91)	2.21 (2.20–2.31)	80 (27–590)	1.9 (1.1–3.3)	$7.52\ (6.89–8.08)\times10^{34}$	3.57 (3.24–4.01)	0.674 (0.518–0.865)	23.8 (6)	18.5 (5)
PuppisA	1.94 (1.68–2.23)	1.88 (1.21–2.19)	2.61 (2.35–3.16)	55 (12–1400)	8.1 (1.9–660)	$2.66\ (2.2–3.07)\times10^{34}$	3.97 (2.93–5.33)	0.689 (0.427–1.25)	7.06 (10)	6.76 (9)
RCW103	1.60 (1.05–1.99)	2.08 (1.42–2.41)	3.80 (2.50–3.96)	6.7 (2.5–2700)	>1.7	$3.46\ (2.76–3.99)\times10^{34}$	2.77 (1.77–4.56)	0.147 (0.0676–0.295)	7.15 (6)	6.02 (5)
RCW86	1.50 (1.33–1.65)	1.51 (1.15–1.73)	2.80 (2.35–3.25)	$3\ (1.4–18)\times10^{3}$	$1.3\ (0.22–3.9)\times10^{3}$	$6.28\ (3.71–8.62)\times10^{33}$	96.5 (43.6–219)	21.2 (11.3–39.2)	12.5 (6)	8.99 (5)
RXJ1713.7-3946	1.69 (1.67–1.71)	1.46 (1.43–1.52)	2.30 (2.30–2.31)	$5.8\ (4.8–6.8)\times10^{3}$	$4.5\ (3.4–5.2)\times10^{2}$	$1.02\ (0.957–1.1)\times10^{34}$	38.7 (35.1–42.8)	10.5 (9.66–11.4)	309 (37)	274 (36)
SN1006	1.78 (1.61–1.92)	1.62 (1.44–1.89)	2.20 (2.05–2.31)	$3\ (1.3–59)\times10^{3}$	$1.6\ (0.14–26)\times10^{2}$	$1.66\ (0.913–2.18)\times10^{33}$	20 (10.6–39.8)	5.64 (3.38–10.1)	17.8 (13)	13.2 (12)
Tycho	2.14 (1.77–2.44)	1.82 (1.02–2.64)	2.31 (2.11–2.71)	>7.2	⋯	$6.15\ (4.97–7.28)\times10^{33}$	2.57 (1.97–3.6)	0.381 (0.191–0.783)	21.3 (8)	16.2 (7)
W51C	2.40 (2.38–2.43)	2.17 (2.08–2.29)	2.50 (2.50–2.51)	$2.3\ (1–6.3)\times10^{3}$	3.5 (2.4–7.9)	$3.85\ (3.76–3.95)\times10^{35}$	2.33 (2.23–2.44)	0.546 (0.522–0.576)	32.5 (16)	18.5 (15)
3C391	2.20 (2.01–2.35)	2.32 (2.20–2.46)	3.31 (2.65–3.96)	28 (10–160)	12 (4.7–180)	$1.92\ (1.76–2.08)\times10^{35}$	2.14 (1.94–2.45)	0.261 (0.188–0.367)	9.58 (6)	8.68 (5)
CTB37A	2.35 (2.29–2.38)	2.52 (2.37–2.69)	2.20 (2.05–2.31)	>6600	45 (3.1–490)	$4.24\ (3.8–4.55)\times10^{35}$	2.81 (2.58–3.19)	0.763 (0.669–0.903)	23.1 (9)	13.9 (8)
G166.0+4.3	1.55 (1.03–2.62)	2.81 (2.20–3.36)	3.90 (3.30–3.96)	<59	4.2 (1.7–16)	$5.95\ (4.34–7.23)\times10^{33}$	1.16 (0.848–1.54)	0.00256 (0.000445–0.021)	10.4 (4)	9.36 (3)
G359.1-0.5	2.37 (2.32–2.40)	2.96 (2.55–3.13)	2.21 (2.15–2.31)	>3200	9 (2.1–29)	$5.06\ (4.69–5.39)\times10^{34}$	2.65 (2.48–2.9)	0.7 (0.627–0.787)	25.1 (4)	8.12 (3)
HB21	2.42 (1.93–2.82)	2.78 (1.00–3.10)	3.30 (3.00–3.96)	5.6 (1.8–150)	⋯	$1.49\ (1.38–1.62)\times10^{34}$	1.09 (0.97–1.27)	0.0252 (0.00962–0.0627)	6.58 (3)	7.4 (2)
HB9	1.61 (1.09–2.34)	2.22 (1.94–2.53)	3.61 (2.85–3.96)	2.6 (1.2–34)	3.1 (1.4–16)	$3.52\ (3.09–4.38)\times10^{32}$	1.46 (1.28–1.81)	0.0124 (0.0024–0.102)	6.34 (4)	6.21 (3)
IC443	2.24 (2.21–2.28)	2.15 (2.06–2.23)	2.70 (2.65–2.80)	$2.3\ (1.2–3.7)\times10^{2}$	8.1 (4.4–24)	$1.28\ (1.25–1.3)\times10^{35}$	2.81 (2.69–2.91)	0.603 (0.558–0.63)	73.2 (21)	38.4 (20)

Table 3
(Continued)

Name	$\Gamma_{\rm cut}$	$\Gamma_{\rm br,low}$	$\Gamma_{\rm br,high}$	$E_{\rm cut}$ (GeV)	$E_{\rm br}$ (GeV)	$L_{1-100\ \rm GeV}$[a]	$\hat{L}$	$R_{\rm GeV}$	χ^2 (d.o.f.)[b]	
									Cutoff	Broken
Kes17	2.25 (1.85–2.49)	2.36 (2.19–2.56)	3.50 (2.45–3.96)	>3.7	⋯	$1.61\ (1.38–1.86) \times 10^{35}$	1.78 (1.56–2.15)	0.162 (0.0618–0.305)	10.6 (6)	7.71 (5)
W28	2.63 (2.60–2.65)	2.71 (2.63–2.75)	2.50 (2.46–2.61)	>4100	23 (1.2–530)	$2.08\ (2.01–2.15) \times 10^{35}$	1.61 (1.54–1.68)	0.306 (0.281–0.333)	28.1 (11)	22.9 (10)
W44	2.19 (2.09–2.34)	2.53 (2.44–2.59)	3.30 (3.10–3.55)	7.4 (5.2–13)	5.1 (2.6–7.5)	$2.1\ (2.05–2.18) \times 10^{35}$	1.47 (1.39–1.54)	0.0632 (0.0523–0.083)	25 (10)	23.1 (9)
W49B	2.40 (2.32–2.45)	2.17 (1.63–2.33)	2.61 (2.60–2.71)	$9.6\ (4.7–22) \times 10^{2}$	6.1 (2.7–540)	$1.16\ (1.08–1.22) \times 10^{36}$	2.26 (2.07–2.63)	0.502 (0.45–0.604)	16.3 (13)	15.4 (12)
CTB33	2.54 (2.30–2.62)	2.57 (2.40–2.69)	1.50 (1.00–3.96)	>9.1	⋯	$1.33\ (1.14–1.45) \times 10^{36}$	1.77 (1.46–2.13)	0.336 (0.125–0.494)	6.55 (2)	5.78 (1)
G150.3+4.5	1.96 (1.82–2.19)	3.79 (3.27–4.00)	1.90 (1.85–2.05)	>370	⋯	$9.4\ (7.32–12.9) \times 10^{32}$	12.3 (2.87–34)	4.05 (1.11–10.7)	7.72 (1)	4.59 (0)
G24.7+0.6	1.99 (1.96–2.03)	2.01 (1.98–2.04)	2.90 (2.65–3.51)	$1.9\ (1.2–3.7) \times 10^{3}$	$5.4\ (3.1–10) \times 10^{2}$	$4.63\ (4.38–4.8) \times 10^{34}$	7.18 (6.51–7.79)	2.08 (1.93–2.24)	79.3 (7)	63.9 (6)
G353.6-0.7	1.50 (1.39–1.64)	1.50 (1.34–1.70)	2.51 (2.35–2.70)	$1.7\ (0.91–3.9) \times 10^{3}$	$5.4\ (2.5–15) \times 10^{2}$	$1.26\ (0.882–1.84) \times 10^{34}$	72.4 (35.6–128)	15.7 (8.94–24.2)	26.3 (21)	22.5 (20)
G73.9+0.9	1.41 (1.02–2.01)	2.41 (1.73–2.77)	3.90 (3.00–3.96)	<6	3.5 (1.2–7.2)	$8.64\ (7.15–9.89) \times 10^{33}$	1.29 (1.04–1.6)	0.00326 (0.000472–0.0149)	7.55 (5)	6.41 (4)
HB3	2.91 (1.96–3.22)	2.90 (2.52–3.32)	2.70 (2.00–3.96)	>1.8	⋯	$9.69\ (7.35–11.3) \times 10^{33}$	1.1 (0.813–1.59)	0.134 (0.0167–0.294)	9.5 (4)	6.16 (3)
Monoceros	2.06 (1.23–2.62)	2.57 (2.23–2.98)	3.90 (3.05–3.96)	3.5 (1.1–310)	>2.3	$8.44\ (6.9–9.83) \times 10^{33}$	1.2 (0.972–1.56)	0.015 (0.00172–0.0466)	10.9 (2)	8.19 (1)
VelaJr.	1.70 (1.64–1.76)	1.72 (1.63–1.78)	2.51 (2.35–2.61)	$4\ (2.8–6.2) \times 10^{3}$	$1.2\ (0.36–2.1) \times 10^{3}$	$1.81\ (1.44–2.07) \times 10^{35}$	32.5 (25.3–44.6)	8.79 (7.19–11.4)	27.7 (15)	22.5 (14)
S147	2.14 (2.00–2.24)	2.18 (2.09–2.26)	3.91 (2.45–3.96)	>21	>1.3	$6.18\ (5.42–6.83) \times 10^{32}$	3.02 (2.59–3.63)	0.566 (0.379–0.826)	12.4 (5)	9.81 (4)
W30	2.56 (2.52–2.59)	2.76 (2.68–2.83)	2.31 (2.15–2.36)	>390	6.7 (4.7–14)	$2.96\ (2.86–3.07) \times 10^{35}$	1.8 (1.69–1.92)	0.376 (0.322–0.419)	52.1 (2)	21.2 (1)
W41	2.25 (2.2–2.29)	1.74 (1.46–1.89)	2.41 (2.40–2.46)	$1.9\ (0.86–4.5) \times 10^{3}$	4.6 (2.4–9.6)	$8.27(7.74–8.89) \times 10^{34}$	3.31 (3.07–3.63)	0.874 (0.801–0.957)	59.4 (13)	33.4 (12)

Notes.
[a] Luminosity in the 1–100 GeV energy range calculated from the best-fit parameters of the exponential cutoff power-law models.
[b] "Cutoff" and "broken" indicate the fit statistics with the cutoff power-law and broken power-law models, respectively.

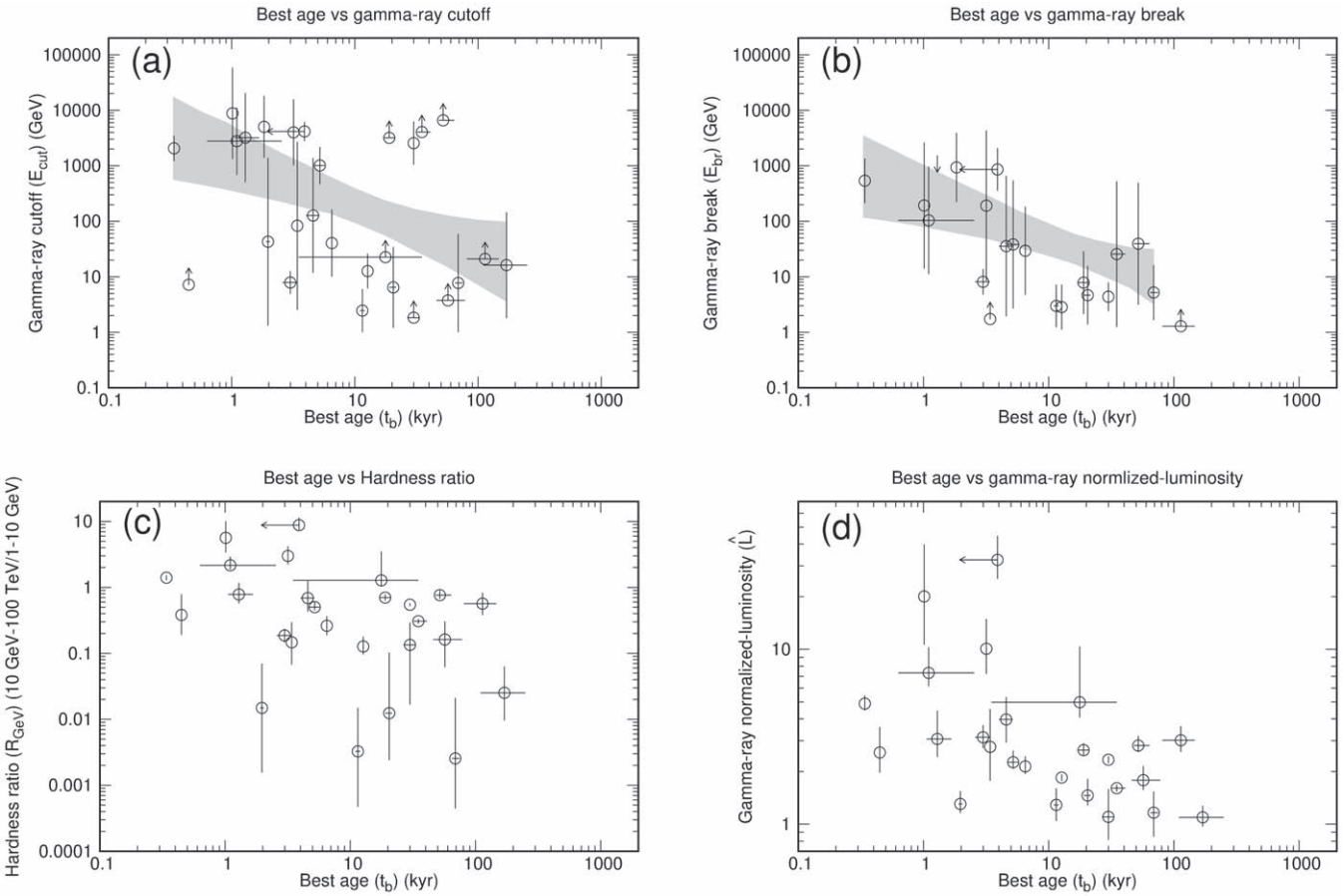

Figure 2. Plots of $E_{\rm cut}$, $E_{\rm br}$, $R_{\rm GeV}$, and $\hat{L}$ over t_b. See Section 2 for the definition of the "best age" t_b. Gray regions represent the best-fit power-law functions and their 1σ confidence ranges.

First, we fit this model to the data and determine the values $E_{\rm bc,br}$ and $E_{\rm bc,cut}$. In this fit, we set a parameter-search range of $\mu_{\rm acc} = 1.5$–2.5 (hereafter, case (A)).[16] The objects with too-good fits (if the null hypothesis probability is higher than 75%) are excluded because their spectra are regarded as being overfitted. The results are shown in Figure 6 with black crosses. Here, meaningful constraints on $E_{\rm bc,cut}$ and $E_{\rm bc,br}$ are obtained only for about a half of the sample. The distributions of $E_{\rm bc,cut}$ and $E_{\rm bc,br}$ are consistent with those of $E_{\rm cut}$ and $E_{\rm br}$, respectively (Figure 2), but are less constrained.

Next, we add additional constraints on the parameter-search ranges based on theories, in order to see how the resultant $E_{\rm bc,br}$ and $E_{\rm bc,cut}$ changes. According to a generalized spectral model composed of both freshly accelerated particles and escaping particles (Ohira et al. 2010, 2011), the spectral index $\mu_{\rm acc}$ is described as

$$\mu_{\rm esc} = \beta/\alpha + \epsilon, \tag{9}$$

where the parameters α, β, and ϵ, respectively, determine the evolution of $E_{\rm bc,br}$ and the particle injection rate, and the energy dependence of the diffusion coefficient around the source. Hereafter, an additional condition, $\mu_{\rm esc} = 2.0$ if $\mu_{\rm acc} < 2.0$, is required (Ptuskin & Zirakashvili 2005; Ohira et al. 2010). We define case (B), with parameter-search ranges of $\mu_{\rm acc} = 1.5$–2.5, $\alpha = 0.5$–3.0, $\beta = 0.0$–1.0, and $\epsilon = 0.0$–1.0. These parameter ranges probably include most of the current theoretical predictions. The results are shown in Figure 6 with red crosses.

Finally, we investigate case (C), in which we assume narrower parameter-search ranges of $\mu_{\rm acc} = 1.5$–2.5, $\alpha = 1.5$–3.0, $\beta = 0.6$ (particle injection by thermal leakage; Malkov & Voelk 1995), and $\epsilon = 0.0$ (without significant emission from escaping particles outside of the source). The range of α is chosen to satisfy $\mu_{\rm esc} = 2.2$–2.4, which is required to explain the spectral index of Galactic cosmic rays (Strong & Moskalenko 1998; Strong et al. 2000; Ptuskin et al. 2006). The results under this condition are also presented in Figure 6 with blue crosses.

Overall, the constraints on $E_{\rm bc,br}$ and $E_{\rm bc,cut}$ are similar for all the three cases (A), (B), and (C). An important finding here is that the distributions of $E_{\rm bc,br}$ and $E_{\rm bc,cut}$ are found to be roughly consistent with those of $E_{\rm cut}$ and $E_{\rm br}$, respectively, and no tighter constraints are obtained.[17] Thus, the conclusion is the same as that simply based on $E_{\rm cut}$ and $E_{\rm br}$. It will be worth trying to quantify the systematic trend of $E_{\rm bc,br}$ as our best guess of the maximum energy $E_{\rm max,\gamma}$ if we have better statistics for quantitative discussions. The spectral indices $\mu_{\rm acc}$ and $\mu_{\rm esc}$ are poorly constrained for all the cases as well. With the observatories such as LHAASO (Cao 2010) and CTA (Cerenkov Telescope Array; Actis et al. 2011), the spectral

[16] This range of $\mu_{\rm acc}$ is selected to explain both the observational gamma-ray index of RX J1713.7−3946 and radio index of Cassiopeia A. The other parameters' ranges are not bounded.

[17] Those with relatively well constrained parameters include "W28-like" and "1713-like" objects defined in Appendix B.

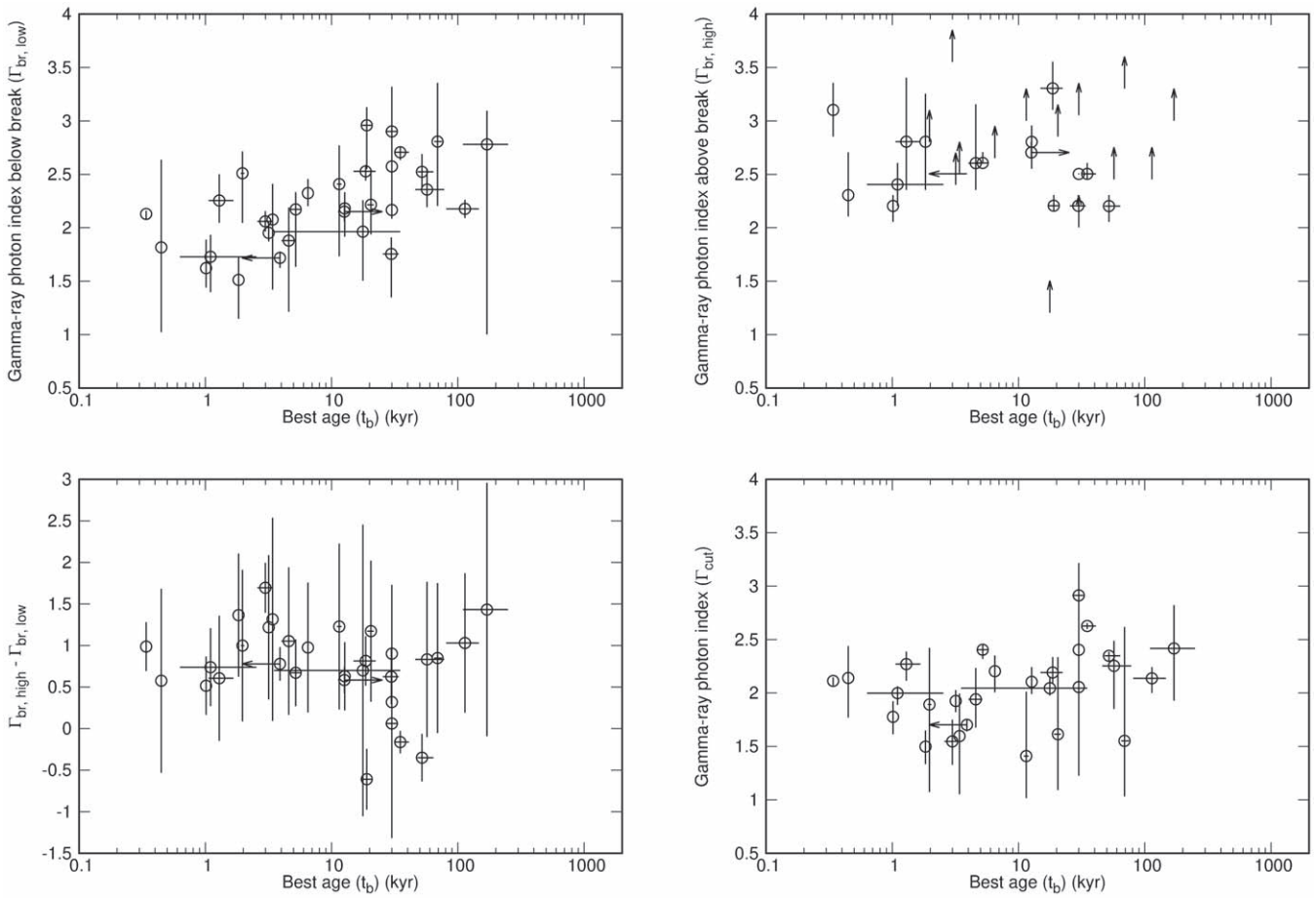

Figure 3. Plots of $\Gamma_{\rm br,low}$, $\Gamma_{\rm br,high}$, their difference, and $\Gamma_{\rm cut}$ over t_b. See Section 2 for the definition of the "best age" t_b.

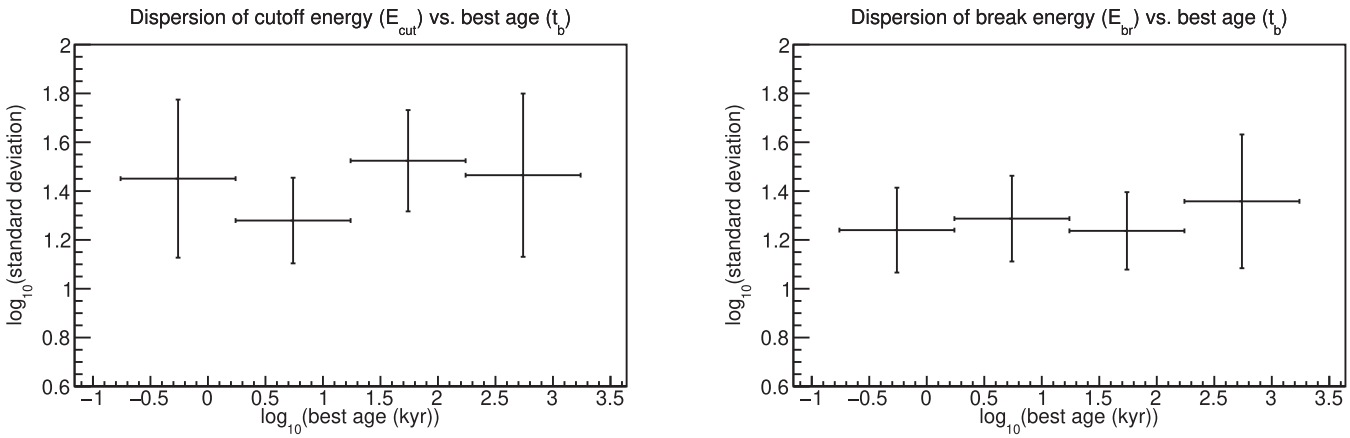

Figure 4. Dispersion of $E_{\rm cut}$ and $E_{\rm br}$ as a function of t_b. See Section 2 for the definition of the "best age" t_b. The logarithmically divided age bins have a ∼1 dex width each, which is close to the uncertainties associated with the ages for most SNRs.

forms and spatial distributions of the gamma-ray-emitting SNRs will be more constrained and thus the contribution of freshly accelerated particles will be more clearly extracted from the data. If we know the absolute energy amount or normalization of the energy distribution of particles emitting gamma-rays, we can get an estimate of the injection parameter β. Such an approach will be possible when the target proton densities for hadronic gamma-ray emission can be estimated reliably for a large number of objects. A recent method on the gas density estimation by Sano et al. (2021b, 2021a) will be promising in this regard.

4.2. Comparison of the Estimated Maximum Energies with Theoretical Calculations

Figure 7 shows comparisons between the observational parameters obtained in Section 3 and several theoretical models. Figure 7 includes analytical models for the maximum energies of the gamma-ray emission in the Bohm limit, the acceleration with wave damping by nonlinear wave–wave interactions caused by shock–ISM (interstellar medium) collisions and the acceleration with the wave damping by

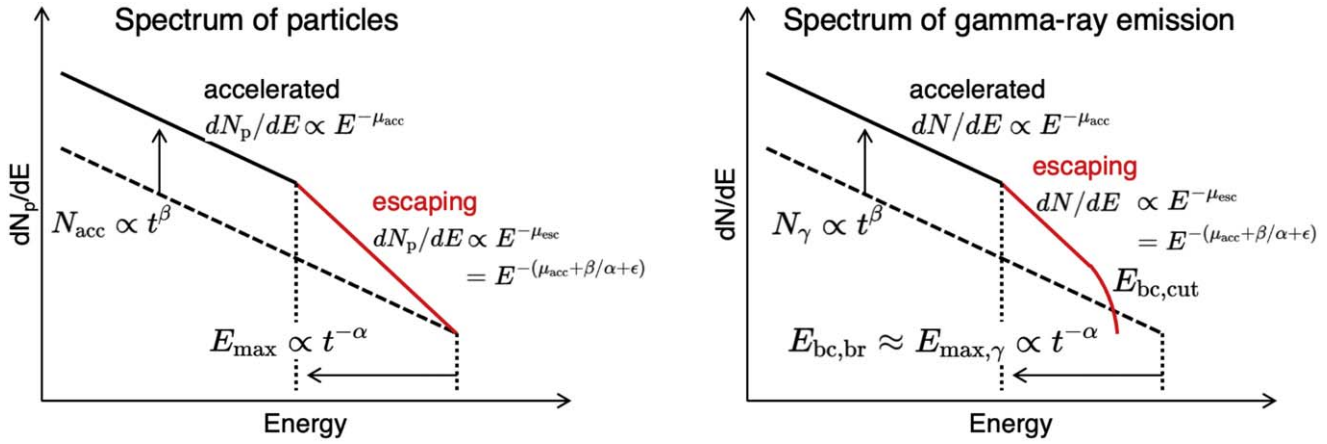

Figure 5. Description of our analytical spectral model for escape-limited particle acceleration (based on Ohira et al. 2010, 2011). Left and right panels describe the energy spectra of accelerated particles and their gamma-ray emission, respectively. Parameters N_{acc}, N_γ, E_{max}, and $E_{max,\gamma}$ represent the normalizations of freshly accelerated particles' and their gamma-rays' energy spectra, and maximum energies of particles and the gamma-rays from them ($E_{max} \approx 10\,E_{max,\gamma}$), respectively. Spectral indices of accelerated and escaping particles are described with μ_{acc} and μ_{esc}, respectively. Physical meanings of α, β, and ϵ are explained in Section 4.2. Break and cutoff energies in the gamma-ray spectrum are indicated with $E_{bc,br}$ and $E_{bc,cut}$.

shock–cloud collisions (Ptuskin & Zirakashvili 2003). These are the maximum energies of accelerated protons multiplied by 0.1 to approximate those of the emission spectra. The three cases include wave amplification by accelerated particles. Note that the wave damping is negligible and the wave amplification by accelerated particles determines the maximum energies in the fast-shock (young-age) limit of the nonlinear wave-damping case. In all the cases, an upstream magnetic field strength (B_0) of 5 μG is assumed. This value is thought to be reasonable at least for SNRs which are older than 2 kyr (e.g., Bamba et al. 2005). In the case of ion-neutral damping, the slowing down of a shock in a cloud is considered to be

$$v_c \approx \frac{v_0}{1 + (n_c/n_0)^{0.5}}, \tag{10}$$

where v_0, v_c, n_0, and n_c are the shock velocities before and after the collision with clouds, and densities of the intercloud region (assumed to be 1 cm^{-3}) and the cloud, respectively (Chevalier 1999). In these models, maximum energies represent exact highest energies which freshly accelerated particles at each time can reach.

Figure 7 includes numerical-calculation results of the maximum energies of accelerated protons with Alfvénic diffusion multiplied by 0.1 obtained by Brose et al. (2020). In this case, the maximum energies are calculated by fitting the time-integrated particle spectra downstream of the shock with an exponential cutoff power-law model, as in the case of the analysis in Section 3. Their calculations include nonlinear wave damping, thus the diffusion coefficient is time-dependent. They only consider the resonant amplification of Alfvénic turbulence by accelerated particles.

Figure 7 also shows numerical calculations of the maximum energies of protons in a uniform ISM case multiplied by 0.1 by Yasuda & Lee (2019). Their simulations assume the Bohm diffusion with $B_0 = 4\,\mu$ G. In this case, the maximum energies represent the exact highest energies that freshly accelerated particles at each time can reach.

From observations, the average time dependence of E_{cut} and E_{br} are found to be $E_{cut} \propto t^{-0.81\pm0.24}$ and $E_{br} \propto t^{-0.77\pm0.23}$ (Section 3). Individual theoretical curves have time dependences of "Bohm (analytical)": $\propto t^{-0.2}$, "Bohm (numerical)": $\propto \sim t^{-0.3}$, "nonlinear (analytical)": $\propto t^{-0.8}$ (in the fast-shock limit) or $\propto t^{-3.8}$ (in the slow-shock limit), "nonlinear (numerical)": $\propto \sim t^{-0.8}$, and "ion-neutral (analytical)": $\propto t^{-1.8}$. Thus, only the nonlinear wave-damping (shock–ISM collision) cases match the observational systematic time-dependence of E_{cut} and E_{br}. Compared to the nonlinear wave-damping models, all the derived parameters, E_{cut}, E_{br}, $E_{bc,cut}$, and $E_{bc,br}$, exhibit similar or slightly smaller values. If the observational values are actually smaller than the theoretical predictions, it might

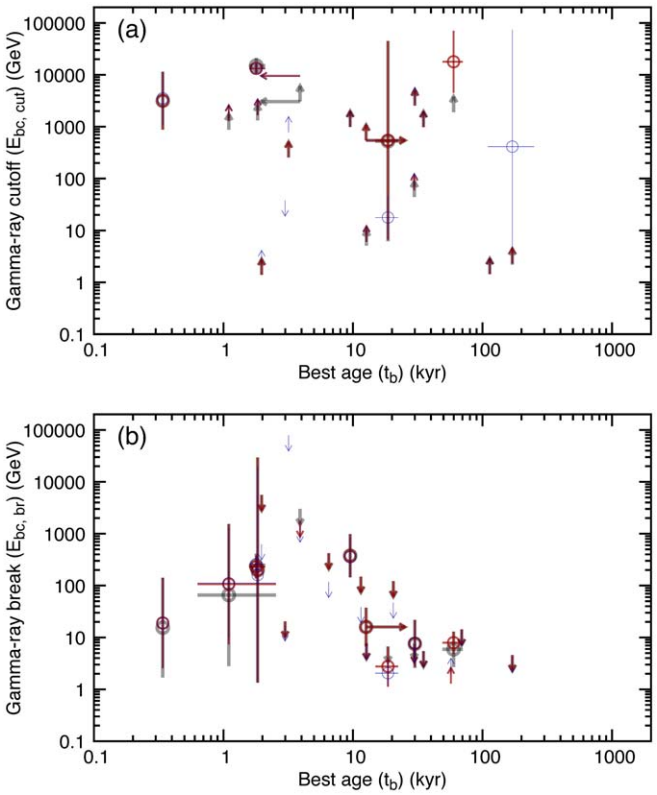

Figure 6. Plots of $E_{bc,cut}$ and $E_{bc,br}$ over t_b. See Section 2 for the definition of the "best age" t_b. Black, red, and blue crosses indicate the three cases (A), (B), and (C), respectively. The conditions for individual cases are explained in Section 4.1.

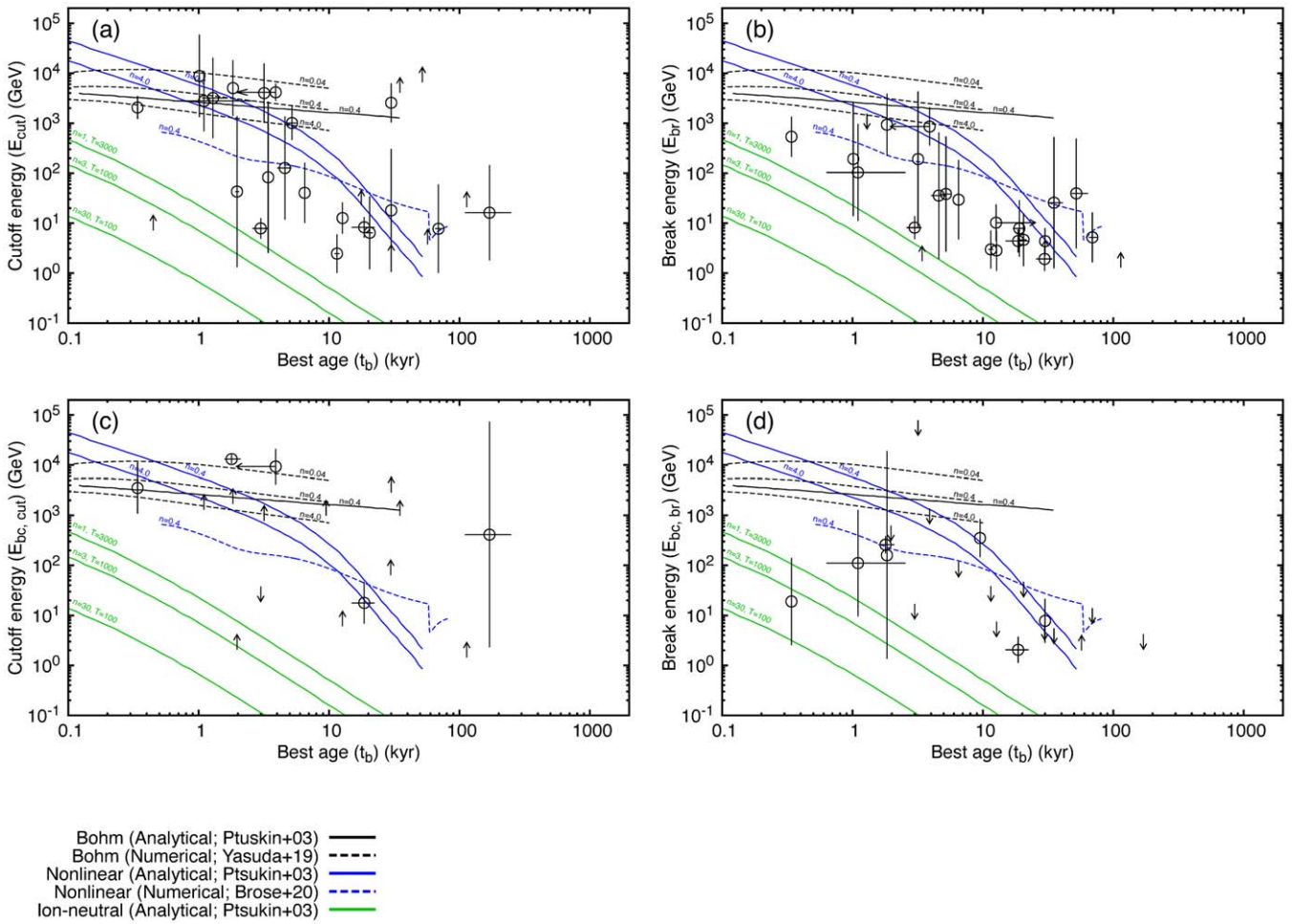

Figure 7. Plots of E_{cut}, E_{br}, $E_{bc,cut}$, and $E_{bc,br}$ over t_b with theoretical calculations. For the parameters $E_{bc,cut}$ and $E_{bc,br}$, the constraints in case (C) are plotted. See Section 2 for the definition of the "best age" t_b. In all the panels, black, blue, and green lines correspond to the Bohm limit, nonlinear damping, and ion-neutral damping models, respectively. The quantities n and T shown beside the model lines stand for the ambient density (cm^{-3}) and temperature (K), respectively. Several cases corresponding to several values of n, which are usually thought to be realistic, are plotted. The ambient density refers to the cloud and ISM density for the "ion-neutral (analytical)" case and for the other cases, respectively. In the case of ion-neutral damping, these values are set to satisfy a condition $nT = 3000$ K cm^{-3} (Wolfire et al. 1995).

suggest that there is a bias that the maximum energies measured from observations are smaller than the highest energies achieved in the systems.[18]

4.3. Are Supernova Remnants PeVatrons?

According to our results for E_{cut}, E_{br}, $E_{bc,cut}$, and $E_{bc,br}$, the maximum energy of the gamma rays from accelerated particles achieved at 1 kyr is $\lesssim$2 TeV. This corresponds to the proton energy of $\lesssim$20 TeV, which is well below PeV. These estimates are consistent with the fact that only a few SNRs are potential PeVatrons according to the recent observations at the energies around PeV (Amenomori et al. 2021; Cao et al. 2021). If the maximum energy during lifetime is attained at a much smaller age, t_M (e.g., Inoue et al. 2021), these estimates can increase to $\lesssim$1 PeV $(t_M/10\,\mathrm{yr})^{-0.8}$ simply based on the measured time dependence of E_{cut} and E_{br}. Also, the actual maximum energies could be larger than our estimates if the possible bias in E_{cut} and E_{br} is taken into account (Section 4.2).

Tsuji et al. (2021) studied the age dependence of the maximum energies of accelerated electrons. They found that the maximum energies increased with time and got highest at $\sim$1 kyr, where an efficient acceleration close to the Bohm limit case seemed to be operating. If protons are accelerated in the same way, they can reach $\sim$100 TeV at 1 kyr (see the theoretical calculations for the Bohm limit case in Figure 7), which is higher than our estimates ($\lesssim$20 TeV). This might be another clue for the potential bias in maximum energies of protons inferred from their gamma-ray emissions.

4.4. Spectral Indices of Accelerated/Released Particles

Spectral indices of freshly accelerated particles, which will be close to $\Gamma_{br,low} = 2.2 \pm 0.4$ or $\Gamma_{cut} = 2.0 \pm 0.4$, are consistent with $\approx$2.0, which is usually predicted by the diffusive shock acceleration theories. Those of escaping particles, which will be close to $\Gamma_{br,high} = 2.9 \pm 0.7$, are also consistent with those required to explain Galactic cosmic rays ($\approx$2.2–2.4; Strong & Moskalenko 1998; Strong et al. 2000; Ptuskin et al. 2006).[19]

[18] Such a bias will be expected, for example, if the gamma-ray-dominant regions are interacting with dense gases and have decelerated shock velocities, so that the maximum energies achieved there are lower than those in the other regions.

[19] SNRs with softer indices $\Gamma_{br,high} > 2.4$ can be explained by the softening due to energy-dependent diffusion around the sources (in other words, due to ϵ; see Section 4.1).

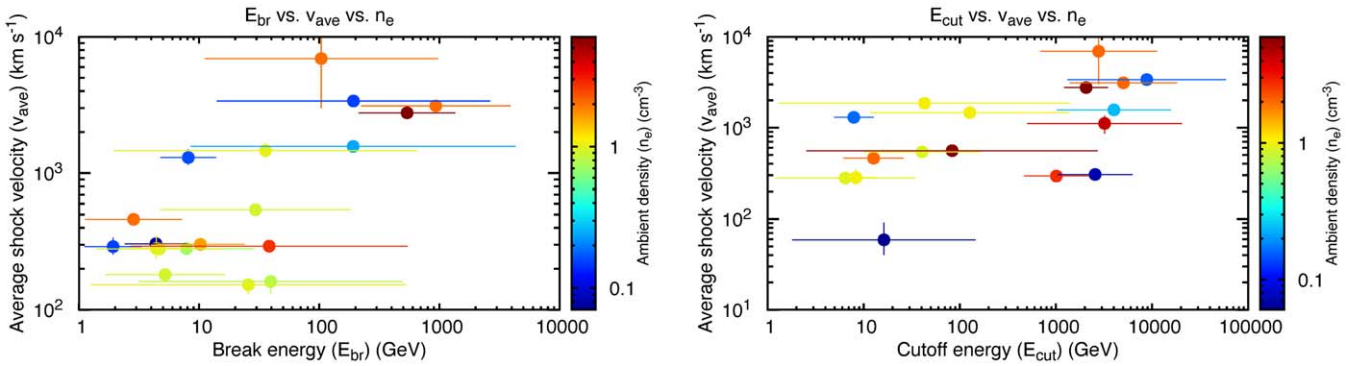

Figure 8. (*left panel*) Scatter plot for the three parameters, break energy $E_{\rm br}$, average shock velocity $v_{\rm ave}$, and ambient density $n_{\rm e}$. (*right panel*) Same for the cutoff energy $E_{\rm cut}$, average shock velocity $v_{\rm ave}$, and ambient density $n_{\rm e}$.

4.5. Average Acceleration Environment of Supernova Remnants

Comparing the time dependence of $E_{\rm cut}$ and $E_{\rm br}$ to the theoretical calculations, we have found that only the shock–ISM collision case with high shock velocities matches the observations (see Section 4.2). Thus, the acceleration regions where the produced gamma rays dominate the total emission will be described with the shock–ISM collision models.

It may be natural to assume that $\alpha \approx 0.8 \pm 0.2$ based on the time dependence of $E_{\rm cut}$ and $E_{\rm br}$. This assumption, however, can be problematic if combined with the natural condition $\beta = 0.6$ (particle injection by thermal leakage), because this combination leads to a condition $\mu_{\rm esc} > \mu_{\rm acc} + 0.6$ and thus the spectral index $\mu_{\rm esc}$ becomes softer than the spectral indices of Galactic cosmic rays (≈2.2–2.4) if $\mu_{\rm acc} \approx 2.0$. We hope that this potential problem will also be addressed with future observations.

It should be noted that SNRs with hadronic gamma-ray emissions are often interacting with dense clouds, and thus the acceleration environments might have to be described by the ion-neutral (shock–cloud) collision models rather than those with the shock–ISM collision (Ptuskin & Zirakashvili 2003, 2005). This might contradict our findings so that some modifications to the inferred acceleration environment might be required (e.g., the presence of clumpy clouds around a shock can be ionized (evaporated) due to shock heating; White & Long 1991; Slavin et al. 2017; Zhang et al. 2019). Numerical calculations of the acceleration and emission including both the high-velocity and low-velocity regions corresponding to thin and thick environments will be helpful.

4.6. Variety of Maximum Energies of Accelerated Particles

The parameters $E_{\rm cut}$ and $E_{\rm br}$ are found to have significant varieties of 1.1–1.8 dex at the same ages (Figure 4). This suggests that the maximum energies during lifetime have certain variety among SNRs. In principle, this is attributed to fundamental parameters such as kinetic energy of supernova explosion, acceleration efficiency, and ambient density. However, the exact form of the maximum energy of freshly accelerated particles at an age t, $E_{\rm max}(t)$, is complicated and dependent on situations around shocks (Ptuskin & Zirakashvili 2003, 2005; Bell et al. 2013; Recchia et al. 2021). As an example, assuming the nonlinear wave-damping case, parameter dependence of $E_{\rm max}(t)$ at a certain age t_0 is

$$E_{\rm max}(t_0) \propto \xi_{\rm CR} v_{\rm sh}^3 \propto \xi_{\rm CR} E_{\rm SN,kin}^{3/5} n_{\rm e}^{-3/5} t_0^{-4/5} \quad (11)$$

in the fast-shock limit and

$$E_{\rm max}(t_0) \propto \xi_{\rm CR}^2 v_{\rm sh}^9 B_0^{-3} \propto \xi_{\rm CR}^2 E_{\rm SN,kin}^{8/5} n_{\rm e}^{-8/5} B_0^{-3} t_0^{-19/5} \quad (12)$$

in the slow-shock limit, where $\xi_{\rm CR}$, $v_{\rm sh}$, $E_{\rm SN,kin}$, $n_{\rm e}$ and B_0 are the acceleration efficiency, shock velocity, kinetic energy of supernova explosion, average ambient density, and the background magnetic field, respectively (Ptuskin & Zirakashvili 2005). The variety of $E_{\rm cut}$ and $E_{\rm br}$ of 1.1–1.8 orders of magnitude is thus easily explained by less than one order-of-magnitude variations of one or more fundamental parameters, and uncertainties associated with the age t_0. As an example, if the parameters $\xi_{\rm CR}$ and $v_{\rm sh}$ are doubled, the maximum energies $E_{\rm max}(t_0)$ change by factors of 16 and 2048 for Equations (11) and 12, respectively.

We investigate the dependence of the break energy $E_{\rm br}$ and cutoff energy $E_{\rm cut}$ on the shock velocity $v_{\rm sh}$ (substituted by $v_{\rm ave} = D/5t_b$) and ambient density $n_{\rm e}$, to identify the cause of such a variety. Figure 8 shows the scatter plots of these parameters. We cannot find the fundamental planes where the break energy $E_{\rm br}$ or cutoff energy $E_{\rm cut}$ can be described as a function of $v_{\rm ave}$ and/or $n_{\rm e}$.[20] This will be at least partly due to inappropriate parameter substitutions (e.g., shock velocities at gamma-ray dominant regions may differ from $v_{\rm ave}$). Such correlation studies will be meaningful if more appropriate estimates of the parameters such as $v_{\rm sh}$ become available.

The difficulty in constraining physical parameters of particle acceleration is largely due to the uncertainty of the spectral index of freshly accelerated particles, $\mu_{\rm acc}$. Thus it may be a good idea to use spectral indices of radio continuum emission as $\mu_{\rm acc}$. However, because the radio spectral indices have spatial variation in a SNR and emission regions for radio and gamma rays may be different, it may be inappropriate to use the radio spectral indices as $\mu_{\rm acc}$. In fact, the radio spectral index of Cassiopeia A (≈2.5) is different from that in the gamma-ray band (≈2.2) (e.g., Abeysekara et al. 2020). Thus, in this work, radio spectral indices are not used. In the future, spatially resolved gamma-ray spectral shapes will be more tightly constrained with larger photon statistics and better angular resolutions (e.g., with CTA).

[20] The positive correlations between $E_{\rm br}$ and $v_{\rm ave}$, and $E_{\rm cut}$ and $v_{\rm ave}$ are due to the correlations between $v_{\rm ave}$ and t_b (Figure 1), $E_{\rm cut}$ and t_b (Figure 2 (a)), and $E_{\rm br}$ and t_b (Figure 2 (b)).

4.7. Contribution of Objects with Possible Inverse-Compton Gamma-ray Emission

In this work, since the gamma-ray spectral models assume hadronic emissions, contamination of objects with inverse-Compton (IC) gamma rays can be problematic. The objects with small $\Gamma_{\rm cut}$ or $\Gamma_{\rm br,low}$ (less than 2.0 at a 1σ significance level, i.e., CTB 37 B; MSH 11-56; RCW 103; RCW 86; RX J1713.7−3946; SN 1006; G353.6−0.7; Vela Jr.; W 41) are possibly emitting gamma rays via IC scattering (e.g., Ohira et al. 2012) and might be unsuitable for this study. However, average trends and variety of the physical parameters constrained in Sections 3 and 4.1 do not change significantly without these objects. And we note that, even for such objects, the maximum energy of protons should be larger than the maximum energy of their gamma rays $E_{\rm max,\gamma}$ because the radiative cooling is effective only for electrons. Thus, the lower limit of the maximum energy of protons can still be obtained.

5. Conclusion

A systematic analysis of 38 gamma-ray-emitting SNRs using their thermal X-ray and gamma-ray properties was performed. A spectral modeling on their gamma-ray spectra was performed to constrain the particle-acceleration parameters. Two candidates of the maximum energy of freshly accelerated particles, the gamma-ray cutoff and break energies, were found to be well below PeV for our sample. We have also tested a simplified spectral model which includes both the freshly accelerated particles and escaping particles to estimate the maximum energies more reliably, but no tighter constraints have been obtained.

The time dependences of the cutoff energy ($E_{\rm cut} \propto t^{-0.81\pm0.24}$) and break energy ($E_{\rm br} \propto t^{-0.77\pm0.23}$) cannot be explained with the simplest acceleration condition of the Bohm limit, and requires shock–ISM collision based on theoretical calculations (Ptuskin & Zirakashvili 2003, 2005; Yasuda & Lee 2019; Brose et al. 2020). The estimated average maximum energies of accelerated particles during lifetime $\lesssim$20 TeV $(t_M/1\ {\rm kyr})^{-0.8}$ are well below PeV if the age at the maximum, t_M, is ∼100–1000 yr. However, if the maximum energy during lifetime is realized at younger ages such as $t_M < 10$ yr, it can become higher to reach PeV. On the other hand, the maximum energies during lifetime are suggested to have a large variety of 1.1–1.8 orders of magnitude from object to object. Although we cannot isolate the cause of such a variety, this work provides an important clue to understand the variety in acceleration environments among SNRs.

We thank the anonymous referee for the valuable comments. We appreciate helpful advice by T. Yoshikoshi, K. Asano, M. Hoshino, M. Teshima, and S. Yamamoto, which has improved the paper significantly. We deeply thank R. Brose and H. Yasuda for providing us with their simulation results. We are grateful to T. Tanaka for his help in the Fermi-LAT data analysis. We appreciate the help by H. Odaka and A. Tanimoto about the Markov Chain Monte Carlo analysis. This research was partially supported by JSPS KAKENHI grant Nos. 19J11069 and 21J00031 (HS), 19K03908 (AB), 18H01232 (RY), 19H01893 (YO); the Grant-in-Aid for Scientific Research on Innovative Areas "Toward new frontiers: Encounter and synergy of state-of-the-art astronomical detectors and exotic quantum beams" (18H05459; AB); Shiseido Female Researcher Science Grant (AB); and Leading Initiative for Excellent Young Researchers, MEXT, Japan (OY). R.Y. deeply appreciates Aoyama Gakuin University Research Institute for helping our research with the fund.

Facility: Fermi-LAT.

Software: HEAsoft (v6.27.2; HEASARC 2014), Fermitools (v1.2.23; https://github.com/fermi-lat/Fermitools-conda/), MCMCLib (https://github.com/kthohr/mcmc).

Appendix A
Fermi-LAT Data Analysis

An analysis of Fermi-LAT data was performed for the SNRs in our sample that satisfied two conditions: those without recent publications (later than 2017) and those without good statistics such that spectral cutoff energies have been determined. The resultant 15 objects, which are listed in Table 4, are the target of this section.

A.1. Data Reduction

For individual objects, the latest Fermi data are obtained from the Pass 8 database.[21] Event data are extracted from a circular region with a radius of 20° centered on the target position. The available time periods for individual sources are shown in Table 4. The extraction energy range is 0.1–300 GeV.

The tools and databases used in the data analysis below are *Fermitools* (v1.2.23)[22] installed through *anaconda* package, the Instrumental Response File version P8R3_SOURCE_V2, the Fermi source list gll_psc_v22.fit (4FGL catalog), the Galactic diffuse background model gll_iem_v07.fits, and the isotropic background model (instrumental and extragalactic) iso_P8R3_SOUCE_V2.txt. Following the recommendation by the Fermi team[23], we applied the event selection: from the SOURCE class, both FRONT and BACK section events are extracted (*evclass = 128 evtype = 3*). Events with zenith angles larger than 90° are rejected from the analysis in order to prevent the contamination from the Earth's bright limb. The energy dispersion correction is enabled for all the model components except for the isotropic background model[24].

A.2. Extraction of Energy Spectra of SNRs with Maximum Likelihood Analysis

The analysis region is a 20° radius circle centered on the SNR position. In order to get energy spectrum of a target source, a binned maximum likelihood analysis based on the spatial and energy distributions of the data is conducted. The spatial bin size is $0.^{\circ}2 \times 0.^{\circ}2$. The data are divided into 35 logarithmic energy bins in the energy range of 100 MeV–300 GeV, which corresponds to ∼10 bins within a decade. The cataloged sources in the analysis region are considered in our analysis basically with fixed spatial and spectral parameters to the cataloged values. Spectral parameters of only those within a $8.^{\circ}5$ radius circle centered on the target source are treated as free parameters.

Most of the target SNRs in this work are included in the 4FGL catalog. For these objects, spectral models for gamma-

[21] https://fermi.gsfc.nasa.gov/cgi-bin/ssc/LAT/LATDataQuery.cgi
[22] https://github.com/fermi-lat/Fermitools-conda/
[23] https://fermi.gsfc.nasa.gov/ssc/data/analysis/documentation/Pass8_usage.html
[24] https://fermi.gsfc.nasa.gov/ssc/data/analysis/documentation/Pass8_edisp_usage.html

Table 4
Fermi-LAT Observation Logs of the 15 SNRs

Supernova Remnant	4FGL Name	Start Date	Stop Date
3C391	4FGL J1849.4-0056	2008-08-04	2012-07-19
		2012-07-19	2016-07-14
		2016-07-14	2020-06-02
CTB109	CTB 109	2008-08-04	2009-12-10
		2009-12-10	2011-04-28
		2011-04-28	2012-09-13
		2012-09-13	2014-01-30
		2014-01-30	2015-06-18
		2015-06-18	2016-11-03
		2016-11-03	2018-01-25
		2018-01-25	2019-03-23
		2019-04-18	2020-06-02
Cygnus Loop	Cygnus Loop	2008-08-04	2009-12-10
		2009-12-10	2011-04-28
		2011-04-28	2012-09-13
		2012-09-13	2014-01-30
		2014-01-30	2015-06-18
		2015-06-18	2016-11-03
		2016-11-03	2018-01-25
		2018-01-25	2019-03-23
		2019-04-18	2020-06-02
G166.0+4.3	…[a]	2008-08-04	2010-02-04
		2010-02-04	2011-08-18
		2011-08-18	2013-02-28
		2013-02-28	2014-09-11
		2014-09-11	2016-03-24
		2016-03-24	2017-10-05
		2017-10-05	2019-01-15
		2019-02-21	2020-06-02
G73.9+0.9	4FGL J2013.5+3613	2008-08-04	2011-01-05
		2011-01-06	2013-06-20
		2013-06-20	2015-12-03
		2015-12-03	2018-03-16
		2018-04-03	2020-06-02
HB9	HB 9	2008-08-04	2010-02-04
		2010-02-04	2011-08-18
		2011-08-18	2013-02-28
		2013-02-28	2014-09-11
		2014-09-11	2016-03-24
		2016-03-24	2017-10-05
		2017-10-05	2019-01-15
		2019-02-21	2020-06-02
Kes17	4FGL J1305.5-6241	2008-08-04	2020-06-02
Kes79	Kes 79	2008-08-04	2012-07-19
		2012-07-19	2016-07-14
		2016-07-14	2020-06-02
Monoceros Nebula	Monoceros	2008-08-04	2014-07-16
		2014-07-17	2020-06-02
MSH11-62	4FGL J1111.8-6039	2008-08-04	2010-07-22
		2010-07-22	2012-07-19
		2012-07-19	2014-07-16
		2014-07-17	2016-07-14
		2016-07-14	2018-07-12
		2018-07-12	2020-06-02
MSH15-56	MSH 15-56 SNR	2008-08-04	2020-06-02
RCW103	…[a]	2008-08-04	2009-12-10
		2009-12-10	2011-04-28
		2011-04-28	2012-09-13
		2012-09-13	2014-01-30
		2014-01-30	2015-06-18
		2015-06-18	2016-11-03
		2016-11-03	2018-03-16
		2018-04-03	2019-05-30
		2019-06-13	2020-09-01
S147	S 147	2008-08-04	2011-08-18
		2011-08-18	2014-09-11
		2014-09-11	2017-08-10
		2017-08-10	2020-06-02
Tycho	4FGL J0025.3+6408	2008-08-04	2020-09-01
W41	W 41	2008-08-04	2020-06-02

Notes. Latest gamma-ray studies for individual objects: Ergin et al. (2014) (3C391); Castro et al. (2012) (CTB109); Katagiri et al. (2011) (Cygnus Loop); Araya (2013) (G166.0+4.3); Zdziarski et al. (2016) (G73.9+0.9); Sezer et al. (2019) (HB9); Gelfand et al. (2013) (Kes17); Auchettl et al. (2014) (Kes79); Katagiri et al. (2016b) (Monoceros Nebula); Slane et al. (2012) (MSH11-62); Temim et al. (2013) (MSH15-56); Xing et al. (2014) (RCW103); Katsuta et al. (2012) (S147); Acciari et al. (2011) (Tycho); H.E.S.S. Collaboration et al. (2015c) (W41).
[a] Not included in the 4FGL catalog.

ray emissions in the catalog are used for the analysis. Two models are included: a power-law model described as

$$\frac{dN}{dE} = N_0 \left(\frac{E}{E_s}\right)^{-\Gamma}, \tag{A1}$$

and a log parabola model described as

$$\frac{dN}{dE} = N_0 \left(\frac{E}{E_s}\right)^{-(a+b\log(E/E_s))}, \tag{A2}$$

where the normalization parameter N_0 and the spectral-shape parameters Γ, a, and b are treated as free parameters, and the energy scale E_s is fixed to certain values. In the 4FGL source catalog, MSH 11−62 is classified as a pulsar wind nebula (Slane et al. 2012; because it contains a pulsar). In this study, considering the possibility that the emission is from the SNR, this object is also included, and the possibility of leptonic gamma-ray emission including other SNRs is discussed in Section 4. For the objects which are not included in the 4FGL catalog (G166.0+4.3 and RCW 103), a log parabola model is used based on an assumption of the hadronic gamma-ray emission. The spatial models for G166.0+4.3 and RCW 103 are selected according to the previous studies on individual objects (Araya 2013; Xing et al. 2014).

A.2.1. Model Fitting for the Entire Energy Range

First, the maximum likelihood analysis is conducted using the model configuration from the 4FGL catalog, and the best-fit source models are obtained. This procedure is repeated with gradually smaller fit tolerance values until the difference of the likelihood from that in the last trial becomes less than unity. Then, in order to

check whether the fitting result is acceptable, the likelihood ratio test is applied. Here, a test statistic (TS) is calculated based on the best-fit model parameters and data. Using a likelihood $\mathcal{L}$ corresponding to a hypothesis H, the TS is defined as

$$\mathrm{TS} \equiv 2\log\left(\mathcal{L}(\mathrm{H}_1)/\mathcal{L}(\mathrm{H}_0)\right), \tag{A3}$$

with H_0 being the null hypothesis in which the best-fit model is assumed and H_1 being a hypothesis in which a point source with only one free parameter (normalization) is added. The TS above is asymptotically distributed as a χ^2 distribution with one degree of freedom (Cash 1979; Mattox et al. 1996), so that the significance of detection $\sigma \approx \sqrt{\mathrm{TS}}$. A TS map is produced by moving a putative point source through a grid of locations on the sky and maximizing the likelihood at each grid point. The resulting TS map represents the residuals remaining. Thus, additional point sources are added at the positions with large residuals, i.e., $\mathrm{TS} > 25$, which approximately corresponds to $>5\,\sigma$ significance. Here, again, the likelihood analysis is done using this updated model configuration. This process is repeated in some cases, to finally get acceptable TS maps.

A.2.2. Model Fitting for Individual Energy Bins

After obtaining an acceptable model configuration, the energy bins of the target SNR are determined. The 100 MeV–300 GeV energy range is divided into 12 logarithmic energy bins, and the likelihood analysis as above is done for each energy bin. In this process, only the normalizations of the target SNR's spectral model and the Galactic and isotropic background models are treated as free parameters (three free parameters in total). For each energy bin, if the significance of the target SNR detection is less than 5σ ($\mathrm{TS} \lesssim 25$), only the upper limit is calculated. The resultant energy spectra of the SNRs are shown in Figures 9 and 10.

A.2.3. Estimation of Systematic Uncertainties

Finally, systematic errors on the target SNR spectra are estimated. Three principal origins of the systematic errors are considered: uncertainties of the LAT effective area and the PSF, and the Galactic diffuse emission model. The $\pm 3\%$ uncertainties of the effective area and $\pm 5\%$ uncertainties of the PSF are assumed according to the LAT performance for the Pass 8 data.[25] The uncertainties of the Galactic diffuse emission model is treated by changing its normalization by $\pm 6\%$ with respect to the best-fit value (originally performed by Abdo et al. 2009 and applied by, e.g., Castro & Slane 2010; Tanaka et al. 2011). It should be noted that this estimation of the uncertainties of the Galactic diffuse emission is different from current standard method, which is comparing several Galactic diffuse emission models (originally performed in de Palma et al. (2013) and applied in, e.g., H.E.S.S. Collaboration et al. 2018; Abdollahi et al. 2020). And our estimates of the uncertainties are probably larger than those with this standard method. The estimated systematic errors on individual energy bins are also shown in Figure 9 and 10 with red solid crosses.

Comparing the individual spectra obtained in this work with the previous studies, we can see that these are consistent with each other in most cases. The spectra obtained in this work show better statistics (the previous works' energy bins with smaller errors than this work's are present in some cases, probably because they did not include the systematic errors which are considered in this work). In the case of e.g., G166.0 +4.3, Kes 79, and MSH 11−62, slight discrepancies can be seen. These are less than a factor of two. Such discrepancies will be explained by the difference in the Galactic diffuse and/or isotropic background models, because different Galactic diffuse background models sometimes yield differences larger than factor of two in fluxes of diffuse sources (de Palma et al. 2013).

[25] https://fermi.gsfc.nasa.gov/ssc/data/analysis/LAT_caveats.html

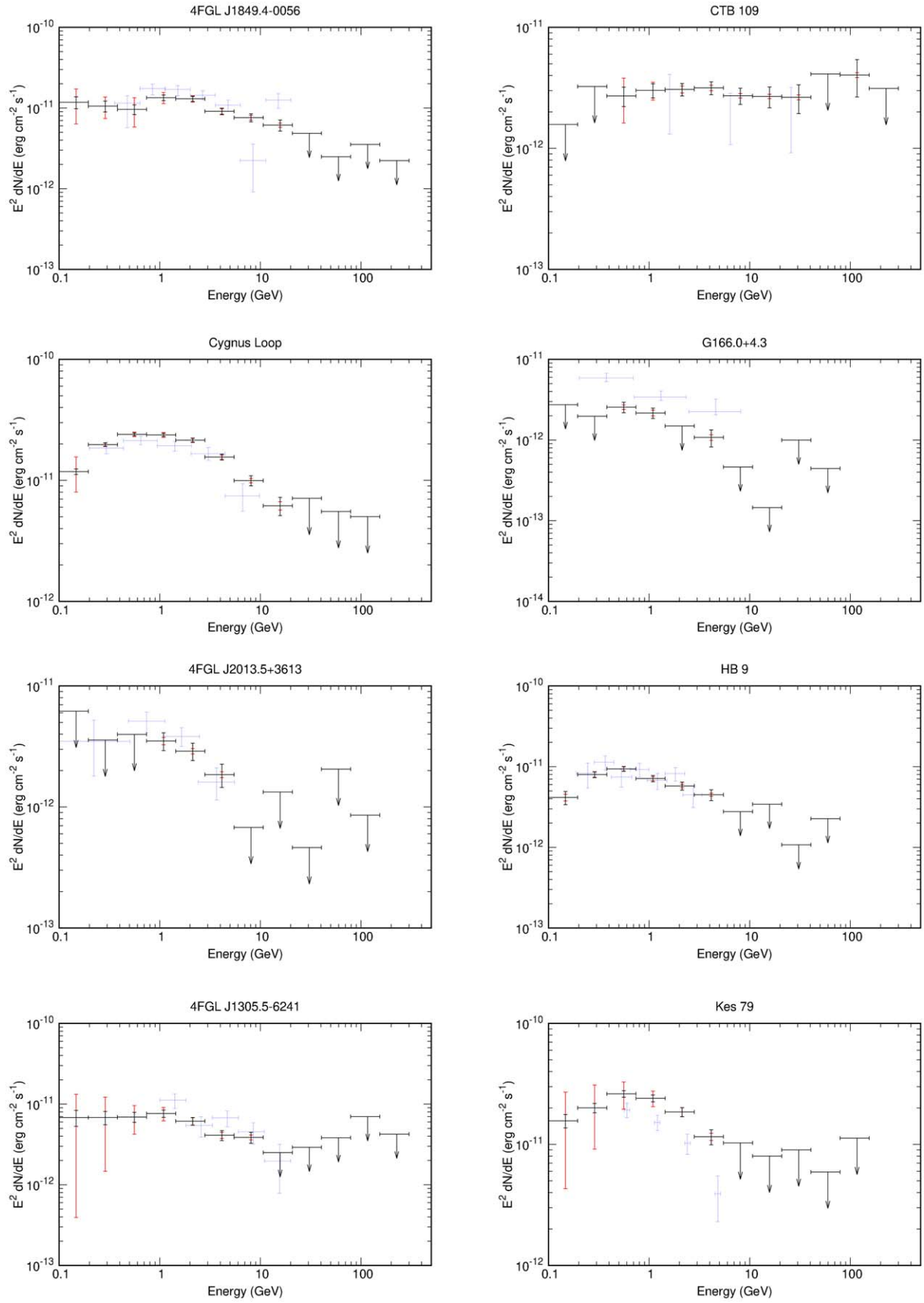

Figure 9. Fermi-LAT energy spectra of the first half of the SNRs listed in Table 4. Black and red crosses represent data points with statistical errors and systematic errors, respectively. Upper limits give 95% confidence levels for energy bins which are undetected with less than 5σ significance. Blue crosses represent the spectra presented in previous works summarized in Table 4.

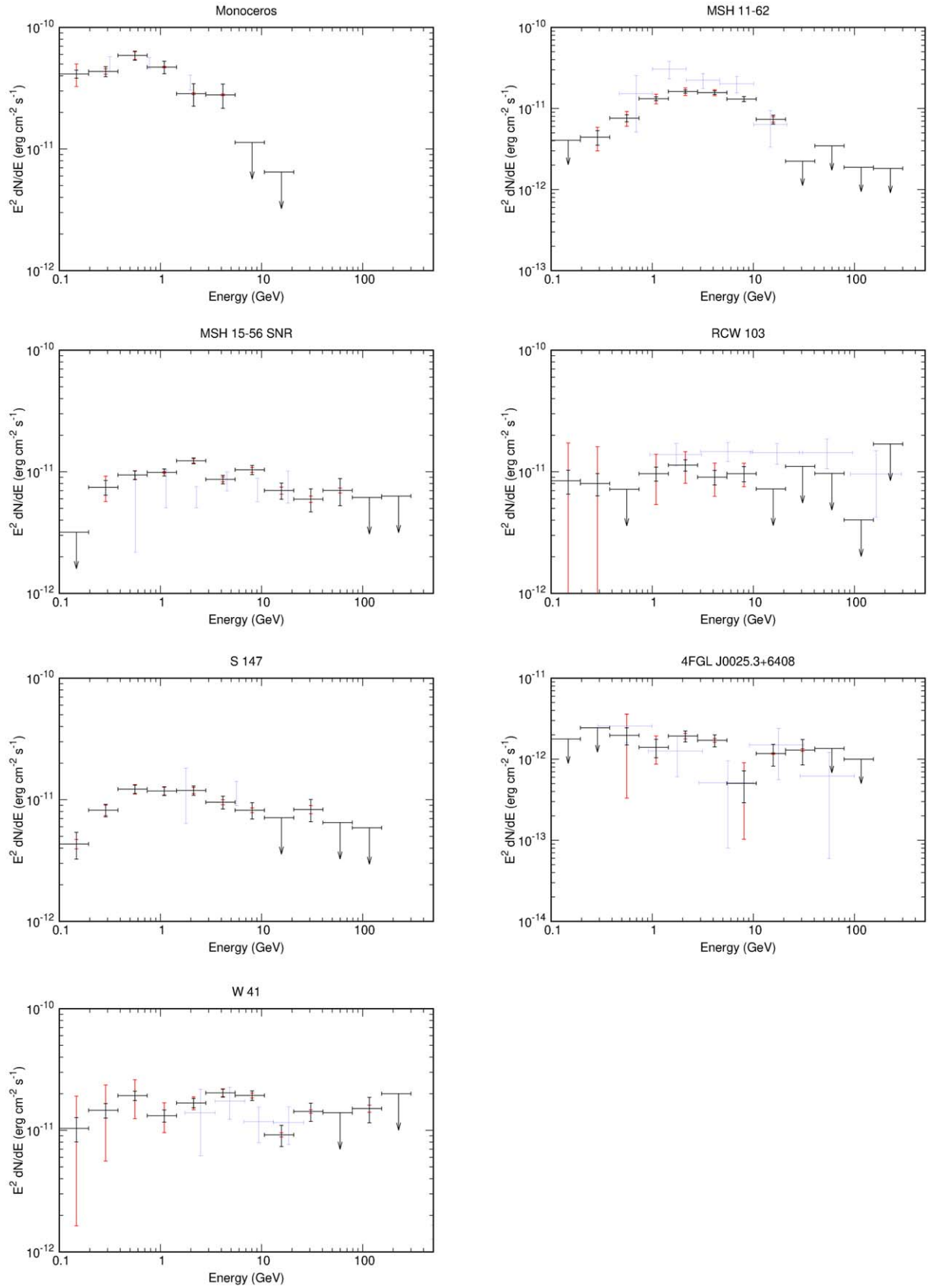

Figure 10. Same as Figure 9, but for the second half of the SNRs listed in Table 4.

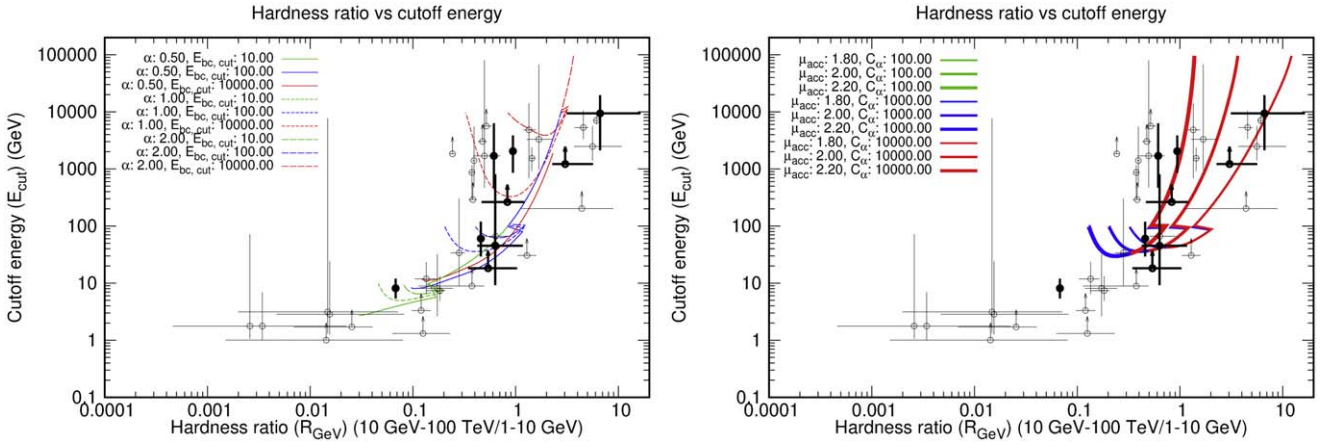

Figure 11. Relation between E_{cut} and R_{GeV} for the data (crosses) and our analytical models (lines). (*left panel*) As for the model curves, different colors and line types indicate different model parameters (α and $E_{bc,cut}$) as specified in the figure. The other parameters are fixed as $\mu_{acc} = 2.0$, $C_\alpha = 100$ GeV, $\beta = 0.6$, and $\epsilon = 0.0$. (*right panel*) Same as the left panel but with different model parameters. Different colors and line types indicate different model parameters (μ_{acc} and C_α) as specified in the figure. The other parameters are fixed as $\alpha = 1.0$, $E_{bc,cut} = 100$ GeV, $\beta = 0.6$, and $\epsilon = 0.0$. For both panels, thick and thin crosses represent the data with and without the reliable ages t_r.

Appendix B
Classification of Gamma-ray-emitting SNRs

Here we compare two observational parameters, gamma-ray cutoff energy E_{cut} and hardness ratio R_{GeV}, with those of our analytical model for escape-limited particle acceleration (Equation (8)) to classify the sample based on their constrained parameters. In this section, we parameterize the break energy as a function of age as $E_{bc,br} = C_\alpha t^{-\alpha}$ in our model. To calculate R_{GeV} and E_{cut} from our analytical model and to compare them with observations, we fit the model spectra with an exponential-cutoff power-law model, as in the case of the observational spectra. In Figure 11, the hardness ratio R_{GeV} is plotted as a function of the cutoff energy E_{cut}. Approximately, ages get larger from top right to bottom left in these plots. Note that our model, in which the cutoff energy $E_{bc,cut}$ is assumed to be time-invariant, may be an extreme case and in reality $E_{bc,cut}$ may change with time significantly.

Regarding the model curves, both the R_{GeV} and E_{cut} basically get smaller with increasing ages, because both of them are governed by $E_{bc,br}$. However, if $E_{bc,cut}$ is fixed to large values such as 10 TeV, E_{cut} visibly increases again after certain ages whereas R_{GeV} continues to decrease (Figure 11). This is because E_{cut} is close to $E_{bc,br}$ in young phases, but after certain ages where a condition $E_{bc,br} \lesssim E_{bc,\,cut}$ is satisfied, it in turn becomes similar to $E_{bc,cut}$. Since the model spectra always get softer with age because escaping particles gradually dominate the emission regardless of whether $E_{cut} \sim E_{bc,br}$ or $E_{cut} \sim E_{bc,\,cut}$, the hardness ratio R_{GeV} always decreases with age. All the model curves plotted in Figure 11 show step-like structures, which are due to such transitions of E_{cut}. Note that such transitions occur in all the cases but are hardly visible in late phases when $E_{bc,cut}$ is small.

Based on Figure 11, we can classify the SNRs into three groups as indicated in Figure 12. The "W 28-like" objects, i.e., W 28, CTB 37 A, G359.0−0.5, W 49 B, W 30, W 51 C, W 41, and G349.7+0.2, are characterized by moderate R_{GeV} with especially large E_{cut}, which will be explained only if the emission is dominated by escaping particles. For these objects, a condition $E_{cut} \sim E_{bc,\,cut}$ is satisfied with large values of $E_{bc,cut}$ as can be seen in Figure 11. The "1713-like" objects, i.e., RX J1713.7−3946, RCW 86, Vela Jr., and G353.6−0.7, are

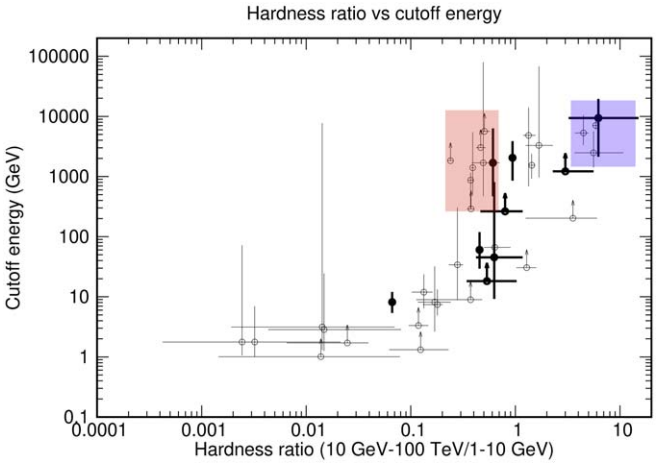

Figure 12. Same as Figure 11 but without the model curves. Two SNR groups, W 28-like group and 1713-like group, are highlighted with red and blue transparent rectangles, respectively.

characterized by especially large R_{GeV} with large E_{cut}, which will be explained only if the spectra are very hard and thus contribution of freshly accelerated particles can be separated well from those of escaping particles. The other objects can be explained by variable parameter sets, so that their parameters are poorly constrained.

ORCID iDs

Hiromasa Suzuki https://orcid.org/0000-0002-8152-6172
Aya Bamba https://orcid.org/0000-0003-0890-4920
Ryo Yamazaki https://orcid.org/0000-0002-1251-7889
Yutaka Ohira https://orcid.org/0000-0002-2387-0151

References

Abdo, A. A., Ackermann, M., Ajello, M., et al. 2009, ApJ, 706, L1
Abdollahi, S., Ballet, J., Fukazawa, Y., Katagiri, H., & Condon, B. 2020, ApJ, 896, 76
Abeysekara, A. U., Archer, A., Benbow, W., et al. 2020, ApJ, 894, 51
Acciari, V. A., Aliu, E., Arlen, T., et al. 2011, ApJL, 730, L20
Acero, F., Aharonian, F., Akhperjanian, A. G., et al. 2010, A&A, 516, A62
Acero, F., Ackermann, M., Ajello, M., et al. 2016, ApJS, 224, 8

Ackermann, M., Ajello, M., Allafort, A., et al. 2013, Sci, 339, 807
Ackermann, M., Ajello, M., Baldini, L., et al. 2017, ApJ, 843, 139
Actis, M., Agnetta, G., Aharonian, F., et al. 2011, ExA, 32, 193
Aharonian, F., Akhperjanian, A. G., Bazer-Bachi, A. R., et al. 2007, ApJ, 661, 236
Aharonian, F., Akhperjanian, A. G., Barres de Almeida, U., et al. 2008a, A&A, 486, 829
Aharonian, F., Akhperjanian, A. G., Barres de Almeida, U., et al. 2008b, A&A, 483, 509
Ahnen, M. L., Ansoldi, S., Antonelli, L. A., et al. 2017, MNRAS, 472, 2956
Ajello, M., Allafort, A., Baldini, L., et al. 2012, ApJ, 744, 80
Aliu, E., Archambault, S., Arlen, T., et al. 2013, ApJ, 770, 93
Ambrogi, L., Zanin, R., Casanova, S., et al. 2019, A&A, 623, A86
Amenomori, M., Bao, Y. W., Bi, X. J., et al. 2021, NatAs, 5, 460
Araya, M. 2013, MNRAS, 434, 2202
Araya, M. 2014, MNRAS, 444, 860
Auchettl, K., Slane, P., & Castro, D. 2014, ApJ, 783, 32
Bamba, A., Yamazaki, R., Yoshida, T., Terasawa, T., & Koyama, K. 2005, ApJ, 621, 793
Bell, A. R. 1978, MNRAS, 182, 147
Bell, A. R., Schure, K. M., Reville, B., & Giacinti, G. 2013, MNRAS, 431, 415
Blair, W. P., Sankrit, R., & Raymond, J. C. 2005, AJ, 129, 2268
Braun, C., Safi-Harb, S., & Fryer, C. L. 2019, MNRAS, 489, 4444
Brose, R., Pohl, M., Sushch, I., Petruk, O., & Kuzyo, T. 2020, A&A, 634, A59
Burrows, D. N., & Guo, Z. 1994, ApJL, 421, L19
Cao, Z. 2010, ChPhC, 34, 249
Cao, Z., Aharonian, F. A., An, Q., et al. 2021, Natur, 594, 33
Caprioli, D., Blasi, P., & Amato, E. 2009, MNRAS, 396, 2065
Carter, L. M., Dickel, J. R., & Bomans, D. J. 1997, PASP, 109, 990
Case, G. L., & Bhattacharya, D. 1998, ApJ, 504, 761
Cash, W. 1979, ApJ, 228, 939
Castro, D., & Slane, P. 2010, ApJ, 717, 372
Castro, D., Slane, P., Carlton, A., & Figueroa-Feliciano, E. 2013, ApJ, 774, 36
Castro, D., Slane, P., Ellison, D. C., & Patnaude, D. J. 2012, ApJ, 756, 88
Caswell, J. L., Murray, J. D., Roger, R. S., Cole, D. J., & Cooke, D. J. 1975, A&A, 45, 239
Celli, S., Morlino, G., Gabici, S., & Aharonian, F. A. 2019, MNRAS, 490, 4317
Cesur, N., Sezer, A., de Plaa, J., & Vink, J. 2019, AdSpR, 64, 759
Chen, Y., & Slane, P. O. 2001, ApJ, 563, 202
Chevalier, R. A. 1999, ApJ, 511, 798
Cohen, J. M. 2016, PhD thesis, Univ. Maryland
Condon, B., Lemoine-Goumard, M., Acero, F., & Katagiri, H. 2017, ApJ, 851, 100
Cristofari, P., Blasi, P., & Amato, E. 2020, APh, 123, 102492
Cui, Y., Yeung, P. K. H., Tam, P. H. T., & Pühlhofer, G. 2018, ApJ, 860, 69
de Palma, F., Brandt, T. J., Johannesson, G., & Tibaldo, L. 2013, arXiv:1304.1395
Doroshenko, V., Pühlhofer, G., Bamba, A., et al. 2017, A&A, 608, A23
Ergin, T., Sezer, A., Saha, L., et al. 2014, ApJ, 790, 65
Ergin, T., Sezer, A., Saha, L., et al. 2015, ApJ, 804, 124
Finley, J. P., & Oegelman, H. 1994, ApJL, 434, L25
Fraija, N., & Araya, M. 2016, ApJ, 826, 31
Fukui, Y., Moriguchi, Y., Tamura, K., et al. 2003, PASJ, 55, L61
Gelfand, J. D., Castro, D., Slane, P. O., et al. 2013, ApJ, 777, 148
Giacani, E., Smith, M. J. S., Dubner, G., et al. 2009, A&A, 507, 841
Giordano, F., Naumann-Godo, M., Ballet, J., et al. 2012, ApJL, 744, L2
Gloeckler, G., & Jokipii, J. R. 1967, ApJL, 148, L41
Green, A. J., Frail, D. A., Goss, W. M., & Otrupcek, R. 1997, AJ, 114, 2058
Green, D. A. 2019a, JApA, 40, 36
Green, D. A. 2019b, A Catalogue of Galactic Supernova Remnants (2019 June version) (Cambridge: Cavendish Laboratory)
Green, D. A., & Stephenson, F. R. 2003, in Historical Supernovae, ed. K. Weiler, Vol. 598 (Heidelberg: Springer), 7
H.E.S.S. Collaboration, Abramowski, A., Aharonian, F., et al. 2015a, A&A, 574, A100
H.E.S.S. Collaboration, Abramowski, A., Aharonian, F., et al. 2015b, A&A, 575, A81
H.E.S.S. Collaboration, Abramowski, A., Aharonian, F., et al. 2015c, A&A, 574, A27
H.E.S.S. Collaboration, Abdalla, H., Abramowski, A., et al. 2018, A&A, 612, A6
Hayato, A., Yamaguchi, H., Tamagawa, T., et al. 2010, ApJ, 725, 894
HEASARC 2014, HEAsoft: Unified Release of FTOOLS and XANADU, Astrophysics Source Code Library, ascl:1408.004
H.E.S.S. Collaboration, Abdalla, H., Abramowski, A., et al. 2018, A&A, 612, A5
Higgs, L. A., Landecker, T. L., & Roger, R. S. 1977, AJ, 82, 718
Hughes, J. P. 2000, ApJL, 545, L53
Hui, C. Y., Seo, K. A., Lin, L. C. C., et al. 2015, ApJ, 799, 76
Hui, C. Y., Yeung, P. K. H., Ng, C. W., et al. 2016, MNRAS, 457, 4262
Hwang, U., Decourchelle, A., Holt, S. S., & Petre, R. 2002, ApJ, 581, 1101
Inoue, T., Marcowith, A., Giacinti, G., van Marle, A. J., & Nishino, S. 2021, ApJ, 922, 7
Jogler, T., & Funk, S. 2016, ApJ, 816, 100
Katagiri, H., Yoshida, K., Ballet, J., et al. 2016a, ApJ, 818, 114
Katagiri, H., Tibaldo, L., Ballet, J., et al. 2011, ApJ, 741, 44
Katagiri, H., Sugiyama, S., Ackermann, M., et al. 2016b, ApJ, 831, 106
Katsuda, S., Tsunemi, H., & Mori, K. 2008, ApJL, 678, L35
Katsuda, S., Acero, F., Tominaga, N., et al. 2015, ApJ, 814, 29
Katsuta, J., Uchiyama, Y., Tanaka, T., et al. 2012, ApJ, 752, 135
Koo, B.-C., Kim, K.-T., & Seward, F. D. 1995, ApJ, 447, 211
Koo, B.-C., & Moon, D.-S. 1997a, ApJ, 475, 194
Koo, B.-C., & Moon, D.-S. 1997b, ApJ, 485, 263
Lagage, P. O., & Cesarsky, C. J. 1983, A&A, 125, 249
Lazendic, J. S., & Slane, P. O. 2006, ApJ, 647, 350
Leahy, D. A. 1989, A&A, 216, 193
Leahy, D. A., & Aschenbach, B. 1995, A&A, 293, 853
Leahy, D. A., Green, K., & Ranasinghe, S. 2013, MNRAS, 436, 968
Leahy, D. A., Naranan, S., & Singh, K. P. 1986, MNRAS, 220, 501
Leahy, D. A., & Tian, W. W. 2008, AJ, 135, 167
Lemoine-Goumard, M., Renaud, M., Vink, J., et al. 2012, A&A, 545, A28
Li, H., & Chen, Y. 2010, MNRAS, 409, L35
Lozinskaya, T. A., Pravdikova, V. V., & Finoguenov, A. V. 2000, AstL, 26, 77
Lozinskaya, T. A., Sitnik, T. G., & Pravdikova, V. V. 1993, ARep, 37, 240
MAGIC Collaboration, Acciari, V. A., Ansoldi, S., et al. 2019, MNRAS, 483, 4578
Malkov, M. A., & Voelk, H. J. 1995, A&A, 300, 605
Marcowith, A., Dwarkadas, V. V., Renaud, M., Tatischeff, V., & Giacinti, G. 2018, MNRAS, 479, 4470
Matsumura, H. 2018, PhD thesis, Kyoto Univ.
Matsumura, H., Uchida, H., Tanaka, T., et al. 2017, PASJ, 69, 30
Mattox, J. R., Bertsch, D. L., Chiang, J., et al. 1996, ApJ, 461, 396
Misanovic, Z., Kargaltsev, O., & Pavlov, G. G. 2011, ApJ, 735, 33
Miyata, E., Tsunemi, H., Pisarski, R., & Kissel, S. E. 1994, PASJ, 46, L101
Moffett, D., Gaensler, B., & Green, A. 2001, in ASP Conf. Ser., Young Supernova Remnants, ed. S. S. Holt & U. Hwang, Vol. 565 (New York: AIP), 333
Moffett, D., Gaensler, B., Green, A., et al. 2002, in ASP Conf. Ser., Neutron Stars in Supernova Remnants, ed. P. O. Slane & B. M. Gaensler, Vol. 271 (San Francisco, CA: ASP), 221
Moffett, D. A., & Reynolds, S. P. 1994, ApJ, 437, 705
Murray, S. S., Fabbiano, G., Fabian, A. C., Epstein, A., & Giacconi, R. 1979, ApJL, 234, L69
Nava, L., Gabici, S., Marcowith, A., Morlino, G., & Ptuskin, V. S. 2016, MNRAS, 461, 3552
Ohira, Y., Kisaka, S., & Yamazaki, R. 2018, MNRAS, 478, 926
Ohira, Y., Murase, K., & Yamazaki, R. 2010, A&A, 513, A17
Ohira, Y., Murase, K., & Yamazaki, R. 2011, MNRAS, 410, 1577
Ohira, Y., Yamazaki, R., Kawanaka, N., & Ioka, K. 2012, MNRAS, 427, 91
Ohnishi, T., Koyama, K., Tsuru, T. G., et al. 2011, PASJ, 63, 527
Okon, H., Uchida, H., Tanaka, T., Matsumura, H., & Tsuru, T. G. 2018, PASJ, 70, 35
Patnaude, D. J., & Fesen, R. A. 2009, ApJ, 697, 535
Pavlović, M. Z., Urošević, D., Vukotić, B., Arbutina, B., & Göker, Ü. D. 2013, ApJS, 204, 4
Petre, R., Kriss, G. A., Winkler, P. F., & Canizares, C. R. 1982, ApJ, 258, 22
Ptuskin, V. S., Moskalenko, I. V., Jones, F. C., Strong, A. W., & Zirakashvili, V. N. 2006, ApJ, 642, 902
Ptuskin, V. S., & Zirakashvili, V. N. 2003, A&A, 403, 1
Ptuskin, V. S., & Zirakashvili, V. N. 2005, A&A, 429, 755
Ptuskin, V. S., Zirakashvili, V. N., & Plesser, A. A. 2008, AdSpR, 42, 486
Radhakrishnan, V., Goss, W. M., Murray, J. D., & Brooks, J. W. 1972, ApJS, 24, 49
Rappaport, S., Doxsey, R., Solinger, A., & Borken, R. 1974, ApJ, 194, 329
Recchia, S., Galli, D., Nava, L., et al. 2021, arXiv:2106.04948
Reed, J. E., Hester, J. J., Fabian, A. C., & Winkler, P. F. 1995, ApJ, 440, 706
Reynoso, E. M., Green, A. J., Johnston, S., et al. 2003, MNRAS, 345, 671
Rosado, M., Ambrocio-Cruz, P., Le Coarer, E., & Marcelin, M. 1996, A&A, 315, 243

Routledge, D., Dewdney, P. E., Landecker, T. L., & Vaneldik, J. F. 1991, A&A, 247, 529
Sano, H., Suzuki, H., Nobukawa, K. K., et al. 2021a, ApJ, 923, 15
Sano, H., Yoshiike, S., Yamane, Y., et al. 2021b, ApJ, 919, 123
Sarma, A. P., Goss, W. M., Green, A. J., & Frail, D. A. 1997, ApJ, 483, 335
Sasaki, M., Heinitz, C., Warth, G., & Pühlhofer, G. 2014, A&A, 563, A9
Sasaki, M., Plucinsky, P. P., Gaetz, T. J., & Bocchino, F. 2013, A&A, 552, A45
Sato, T., Koyama, K., Takahashi, T., Odaka, H., & Nakashima, S. 2014, PASJ, 66, 124
Schure, K. M., & Bell, A. R. 2013, MNRAS, 435, 1174
Sezer, A., Ergin, T., Yamazaki, R., Sano, H., & Fukui, Y. 2019, MNRAS, 489, 4300
Slane, P., Chen, Y., Lazendic, J. S., & Hughes, J. P. 2002, ApJ, 580, 904
Slane, P., Hughes, J. P., Edgar, R. J., et al. 2001, ApJ, 548, 814
Slane, P., Hughes, J. P., Temim, T., et al. 2012, ApJ, 749, 131
Slavin, J. D., Smith, R. K., Foster, A., et al. 2017, ApJ, 846, 77
Sollerman, J., Ghavamian, P., Lundqvist, P., & Smith, R. C. 2003, A&A, 407, 249
Strong, A. W., & Moskalenko, I. V. 1998, ApJ, 509, 212
Strong, A. W., Moskalenko, I. V., & Reimer, O. 2000, ApJ, 537, 763
Sun, M., Seward, F. D., Smith, R. K., & Slane, P. O. 2004, ApJ, 605, 742
Suzuki, H., Bamba, A., Enokiya, R., et al. 2020a, ApJ, 893, 147
Suzuki, H., Bamba, A., Nakazawa, K., et al. 2018, PASJ, 70, 75
Suzuki, H., Bamba, A., & Shibata, S. 2021, ApJ, 914, 103
Suzuki, H., Bamba, A., Yamazaki, R., & Ohira, Y. 2020b, PASJ, 72, 72
Tanaka, T., Allafort, A., Ballet, J., et al. 2011, ApJL, 740, L51
Temim, T., Slane, P., Castro, D., et al. 2013, ApJ, 768, 61
Tian, W. W., & Leahy, D. A. 2011, ApJL, 729, L15
Tian, W. W., & Leahy, D. A. 2012, MNRAS, 421, 2593
Tian, W. W., & Leahy, D. A. 2014, ApJL, 783, L2
Tian, W. W., Li, Z., Leahy, D. A., & Wang, Q. D. 2007, ApJL, 657, L25
Troja, E., Bocchino, F., Miceli, M., & Reale, F. 2008, A&A, 485, 777
Tsuji, N., & Uchiyama, Y. 2016, PASJ, 68, 108
Tsuji, N., Uchiyama, Y., Khangulyan, D., & Aharonian, F. 2021, ApJ, 907, 117
Uchida, H., Koyama, K., Yamaguchi, H., et al. 2012, PASJ, 64, 141
Wang, S., Zhang, C., Jiang, B., et al. 2020, A&A, 639, A72
Washino, R., Uchida, H., Nobukawa, M., et al. 2016, PASJ, 68, S4
White, R. L., & Long, K. S. 1991, ApJ, 373, 543
Williams, B. J., Blair, W. P., Blondin, J. M., et al. 2011, ApJ, 741, 96
Winkler, P. F., Gupta, G., & Long, K. S. 2003, ApJ, 585, 324
Winkler, P. F., Tuttle, J. H., Kirshner, R. P., & Irwin, M. J. 1988, in IAU Colloq. 101: Supernova Remnants and the Interstellar Medium, ed. R. S. Roger & T. L. Landecker (Cambridge: Cambridge Univ. Press), 65
Winkler, P. F., Williams, B. J., Reynolds, S. P., et al. 2014, ApJ, 781, 65
Wolfire, M. G., Hollenbach, D., McKee, C. F., Tielens, A. G. G. M., & Bakes, E. L. O. 1995, ApJ, 443, 152
Xin, Y.-L., Liang, Y.-F., Li, X., et al. 2016, ApJ, 817, 64
Xing, Y., Wang, Z., Zhang, X., & Chen, Y. 2014, ApJ, 781, 64
Yamaguchi, H., Koyama, K., Katsuda, S., et al. 2008, PASJ, 60, S141
Yamauchi, S., Minami, S., Ota, N., & Koyama, K. 2014, PASJ, 66, 2
Yasuda, H., & Lee, S.-H. 2019, ApJ, 876, 27
Yuan, Q., Huang, X., Liu, S., & Zhang, B. 2014, ApJL, 785, L22
Zdziarski, A. A., Malyshev, D., de Oña Wilhelmi, E., et al. 2016, MNRAS, 455, 1451
Zeng, H., Xin, Y., & Liu, S. 2019, ApJ, 874, 50
Zhang, G.-Y., Slavin, J. D., Foster, A., et al. 2019, ApJ, 875, 81
Zhao, H., Jiang, B., Li, J., et al. 2020, ApJ, 891, 137
Zhou, P., & Vink, J. 2018, A&A, 615, A150